CHARACTERIZATION OF A HIGH-PRESSURE BURNER USING CHEMILUMINESCENCE, OH-PLIF AND THERMOMETRY

A Thesis

by

WILLIAM EVERETTE SWAIN

Submitted to the Office of Graduate and Professional Studies of
Texas A&M University
in partial fulfillment of the requirements for the degree of

MASTER OF SCIENCE

Chair of Committee,	Waruna Kulatilaka
Committee Members,	Eric Petersen
	Rodney Bowersox
Head of Department,	Andreas A. Polycarpou

May 2021

Major Subject: Mechanical Engineering

ABSTRACT

Most practical propulsion and power generation systems based on gas turbine engines operate at elevated combustor pressures. For example, the turbine inlet pressures of modern gas turbine engines used in airplanes typically vary between 30–50 bar. Therefore, innovative diagnostics methods are needed to understand the temporally and spatially resolved flame dynamics inside combustors at high pressures in order to increase the combustion efficiency and flame stability, and also reduce pollutant formations. Hence, the objective of this thesis research is to establish a laboratory-scale high-pressure burner facility suitable for incorporating non-intrusive, spatially, and temporally resolved optical diagnostics up to pressures of 50 bar. The high-pressure facility and the development of the supporting engineering systems are discussed in detail. High-speed chemiluminescence imaging of OH* and CH* is used to characterize and reduced flame instabilities. Following these studies, a stainless-steel disk was mounted above the burner surface to stabilize the flames. Subsequently, the laser diagnostics method, hydroxyl radical planar laser-induced fluorescence (OH-PLIF) imaging, is used to study the spatially resolved flame structure, combustion zones, and temperature distribution in the high-pressure flames. The flames studies are premixed CH_4/air mixtures with equivalence ratios ranging from 0.7–1.3. Initial experiments were conducted up to pressures of 10 bar. Laser pulses of approximately 10-ns duration at the wavelength of 283.305 nm were used to excite the $Q_1(7)$ rotational line of the $A^2\Sigma^+ \leftarrow X^2\prod$ (1, 0) band of the OH radical, followed by fluorescence detection from the A←X (1, 1) and (0,0) bands. Also, the $Q_1(5)$ and $Q_1(14)$ rotational lines of the OH radical were used for two-color OH-PLIF thermometry measurements. The laser energy dependence and the effects of collisional quenching on the measured fluorescence signal interpretation at elevated pressures are discussed. The OH

radical number density distributions are compared with equilibrium flame calculations in the range of flame equivalence ratios from 0.8–1.2. The present study establishes a robust burner configuration for high-pressure combustion studies such as soot and NOx formation, as well as a testbed for advanced optical diagnostic development using nonlinear spectroscopic techniques.

ACKNOWLEDGEMENTS

I would like to thank my advisor Dr. Waruna Kulatilaka for his continued support and faith in me throughout this process. He has been a great mentor, and I have learned much from him throughout my career at Texas A&M. First throughout my undergraduate degree, and then as my graduate thesis advisor. He has been instrumental in my development professionally and academically and is someone I view as a role model. His attention to detail and constant support have made all this possible and I want to sincerely thank him for taking a chance on me. I also want to thank Drs. Eric Petersen and Rodney Bowersox for serving on my committee and providing numerous guidance and advice during this study.

Secondly, I want to thank Yejun Wang for his patience and guidance in guiding me throughout the process of conducting the experiments and technical advice in various areas. Thanks also to Pradeep Parajuli, Matt Hay, and Will Weinert for their assistance with the burner project and contributions to the team. Thanks to Mr. Carl Johnson at the Turbomachinery Laboratory for providing technical support and assistance with machining. Also, a thank you to Mr. Jim Mabe for his assistance on the coding and electronics portion, as without his contribution, it would not have been possible to complete this work.

Special thanks go out to my wife, friends, and family for their continued encouragement throughout both my undergraduate and now graduate studies. This work simply would not have been possible without their unconditional love and support.

CONTRIBUTORS AND FUNDING SOURCES

Contributors

This work was supervised by a thesis committee consisting of Professors Waruna Kulatilaka and Eric Petersen of the J. Mike Walker ’66 Department of Mechanical Engineering and Professor Rodney Bowersox of the Department of Aerospace Engineering.

Yejun Wang and Pradeep Parajuli contributed to the experiments by providing key assistance in developing the `PLIF laser diagnostics system as well as conducting PLIF experiments.Preadeep Parajuli performed numerical simulations of the flames and Yejun Wang performed signal quenching corrections. Matt Hay and William Weinert also helped with some chemiluminescence data taking and analysis.

All other work conducted for the thesis (or) dissertation was completed by the student independently.

Funding Sources

This work was made possible in part by the National Science Foundation (NSF), Combustion, Fire and Plasma Systems Program, Award # CBET-1604633. The facilities support from the Texas A&M Engineering Experimental Station Turbomachinery Laboratory (TEES-TL) is also highly acknowledged. The contents of this thesis are solely the responsibility of the author and do not necessarily represent the official views of the above agencies.

TABLE OF CONTENTS

Page

LIST OF FIGURES

1. INTRODUCTION

1.1. Background

Gas turbine engines are an integral part of the modern industrialized world. Used in airplanes, oil and gas, and power generation industries, these engines are critical for activities in our everyday life. Increasing efficiency and reducing harmful emissions are the two main areas of improvement for gas turbine engines. Higher inlet temperatures, better materials, and cooling methods can contribute to increasing efficiency [1]. Decreasing carbon dioxide emissions in these systems will directly lead to reduced pollutant output on a significant scale. Even minor increases in thermal efficiency or decreases in pollutant formation can pay substantial dividends in the aircraft and power generation industries. Gas turbine engines typically operate in the pressure range of 30–50 bar. However, most research findings related to hydrocarbon combustion processes are focused on atmospheric-pressure flames. While this data is valuable, it cannot be directly extended to practical combustion applications as the latter often operate at higher pressures, as mentioned previously. Naturally, the need for more experimental data at these higher pressures must be addressed in order to provide more realistic results for these combustion processes. The most feasible way of exploring these processes in a research laboratory setting is through the development of optically accessible high-pressure burners and implementing advanced laser diagnostics.

1.2. Related Work

High-pressure burners are unique experimental tools used to simulate combustion processes inside gas turbine engines and other stationary power generation applications. The basic concept is to place a flame, often a flat flame burner, inside a large pressure vessel with the required mechanical characteristics to operate at higher pressures. The critical challenge in these burners is creating a stable flame and ensuring sufficient optical window properties to facilitate optical and

laser diagnostics. Non-intrusive laser diagnostics is currently the most accurate method for obtaining information about combustion processes. Several institutions have already started experiments at both low and high pressures implementing laser diagnostics [2–8]. The focus of these studies has been centered on efforts to increase efficiency and decrease emissions [9]. The results have been promising in replicating accurate flame conditions, but laser diagnostic techniques still need to be developed to provide an accurate representation of the combustion processes. Purdue University and the German Aerospace Agency (DLR) conducted an experiment at 5 bar in 2015 using simultaneous particle image velocimetry (PIV) and hydroxyl radical planar laser-induced fluorescence (OH-PLIF) imaging. This study applied these techniques simultaneously to show the interaction between the turbulent flow field and the flame structure. The main issues noted were signal degradation due to absorption and surface reflections, pressure broadening of different molecular transitions that naturally occur at higher pressures, decreased OH mole fractions, and non-radiative losses of the fluorescence signal due to collision with other particles [10]. The experimental results for OH PLIF yielded a substantial difference in the OH signal from one side of the combustion chamber to the other. They were significantly different from previous measurements taken at atmospheric pressures, which yielded more symmetric and theoretically predictable data. This study helped to illustrate some of the current issues with high-pressure combustion diagnostics and the challenges of reproducing theoretically consistent data without the need for applying extensive correction factors. In the context of these general issues with high-pressure combustion, the present work is focused on chemiluminescence and OH-PLIF measurements in the TAMU high-pressure burner facility.

1.3. Significance of Thesis Research

The research included in this thesis covers the development of a high-pressure burner facility and conducting optical and laser diagnostics, including chemiluminescence, OH-PLIF, and thermometry. The primary motivation behind the thesis research was to characterize a high-pressure burner for further laser diagnostics. The laser diagnostic techniques performed were conventional techniques that had been previously used but were not tested extensively at higher pressures. Chemiluminescence laser diagnostics were employed to ensure the stability of the flame and provide a preliminary volume-averaged representation of the CH* and OH* radical zones. Minimizing the flame oscillations was crucial as the data could not be reported to be valid unless the flame was stable, which would allow for accurate representation by numerical calculations under different conditions. A high-speed camera with bandpass filters for CH* at 434 ± 17 nm, OH* at 315 ± 15 nm was set up in front of the facility and recorded at a rate of 1 kHz (or 1000 images per second). The initial data with the open flame revealed a need for a stabilization disk because stabilizing the flame was one of the inherent problems with high-pressure experiments. After the disk was added, a significant decrease in the overall fluctuations was noted, and the data were determined to be consistently reproducible.

The CH* radicals decreased as the pressure increased, and they were concentrated around the surface of the burner. However, the OH* radicals increased as the pressure and equivalence ratios increased. These radicals showed an even distribution between the burner surface and the bottom of the flame stabilization disk. This study helped to validate the feasibility of conducting further experiments and helped to increase the understanding of flame conditions at higher pressures. However, this process should be viewed as a preliminary step as the chemiluminescence can only offer volume-averaged representations of the flame. The second round of experimentation

consisted of OH-PLIF measurements inside the combustion chamber using the stabilization disk. A Nd:YAG laser was used to excite the $Q_1(7)$ rotational line of the $A^2\Sigma^+ \leftarrow X^2\prod$ (1, 0) band of the OH radical. These measurements yielded a two-dimensional image of the flame and an accurate representation of the flame structure. The OH radical signal decreased as the pressure increased, in large part due to collisional quenching effects and fluorescence trapping.

Therefore, it is best to view this dissertation as a proof-of-concept study that validated the operation of the high-pressure burner facility for further complex measurements with advanced laser diagnostics. Stability, flame structure, and temperature distribution are documented in this thesis, and the combustion conditions at high pressures can be applied to real-world scenarios.

1.4. Thesis Outline

This thesis consists of five chapters. Chapter II consists of a literature review that covers existing high-pressure burners at several leading research institutions as well as chemiluminescence and OH PLIF imaging diagnostics. Chapter III documents the high-pressure burner facility in its entirety. This chapter includes the design, hardware, and experimental validation to ensure the safety of the operators throughout the process. Chapter IV explores the high-speed chemiluminescence portion of the experiments conducted on the burner. The theory and experimental apparatus and the results from a study that focuses on the concentration of the OH* and CH* radicals and the stabilization of the flame through the addition of a flame stabilization disk are presented. Chapter V focuses on the OH-PLIF imaging experimental apparatus, results, and discussion of flame structure and thermometry. Chapter V also discusses quenching and other interferences that occur at higher pressures, which also helps to prove the motivation and significance of the research being conducted. Conclusions from the experiments and possibilities for future work are discussed at the end of Chapter VI.

2. LITERATURE REVIEW

2.1 High-Pressure Combustion Devices

High-pressure combustion, as mentioned previously, is an ongoing area of interest in the combustion community. Measurements at higher pressure facilities require advanced engineering methods for safe operation and experimentation. Different research institutions use unique facilities, but they generally have several components in common, which allow for safe operation at these higher pressures. These components include a burner or combustion system that generates a flame, an optical access points for laser diagnostics that usually consists of high-grade optical windows, control and safety systems for proper operation, a translation system to adjust the height of the combustion event, and a pressure vessel that encloses the burner to sustain the pressure throughout the experiment. Several burners from other universities are discussed below in detail. Stanford University researchers conducted nitric oxide laser-induced fluorescence in a high-pressure system, as shown in Fig. 1. The burner incorporates many of the systems described above. Optical windows for laser diagnostic measurements, which provide access for non-intrusive laser diagnostics, were made of quartz. The pressure vessel is made from 316 stainless steel mounted on a translational mechanism that allows the entire burner mechanism to translate up and down in order for different orientations during laser diagnostic experiments. A premixed methane and air flat flame burner was enclosed inside the pressure vessel, producing a flame similar to the TAMU high-pressure burner facility.

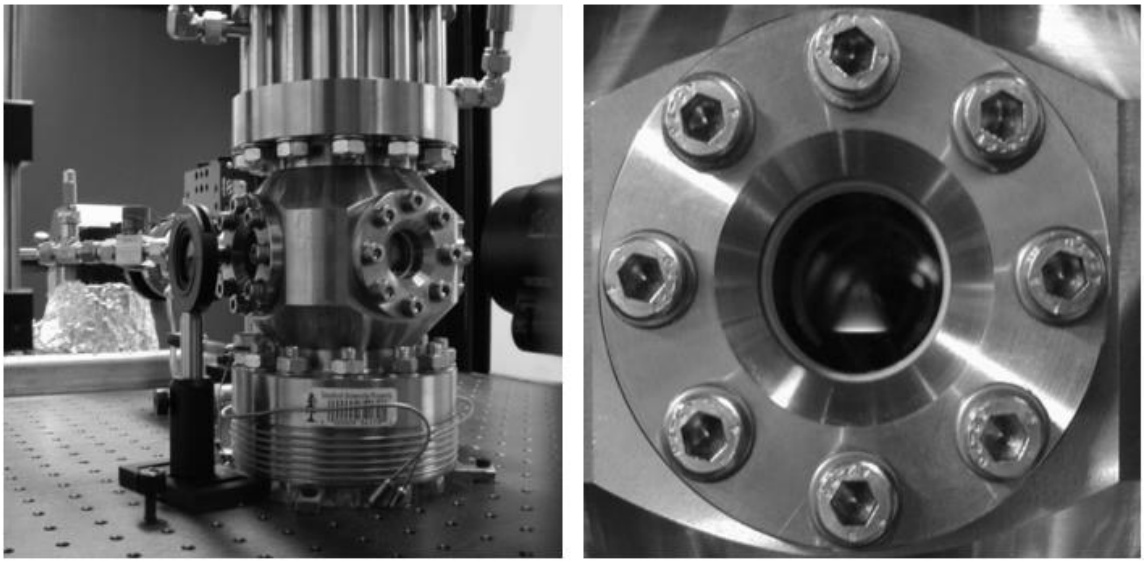

Fig. 1: The High-Pressure Burner at Stanford reprinted from [11]

The physical components of the burner are important, but the engineering systems involved are what make the safe and efficient operation. A detailed schematic of the Stanford methodology is shown in Fig. 2. The mass flow controllers provide gases into the combustion vessel at the desired flow rates and pressures. The exhaust system back regulates the flow output by shutting the valve at the top based on the feedback signal from the pressure transducer. A computer controls the electrical components of the facility and provides accurate data acquisition as well. The Stanford system is very similar to the system employed by TAMU and to many of the fundamentals discussed later in this work.

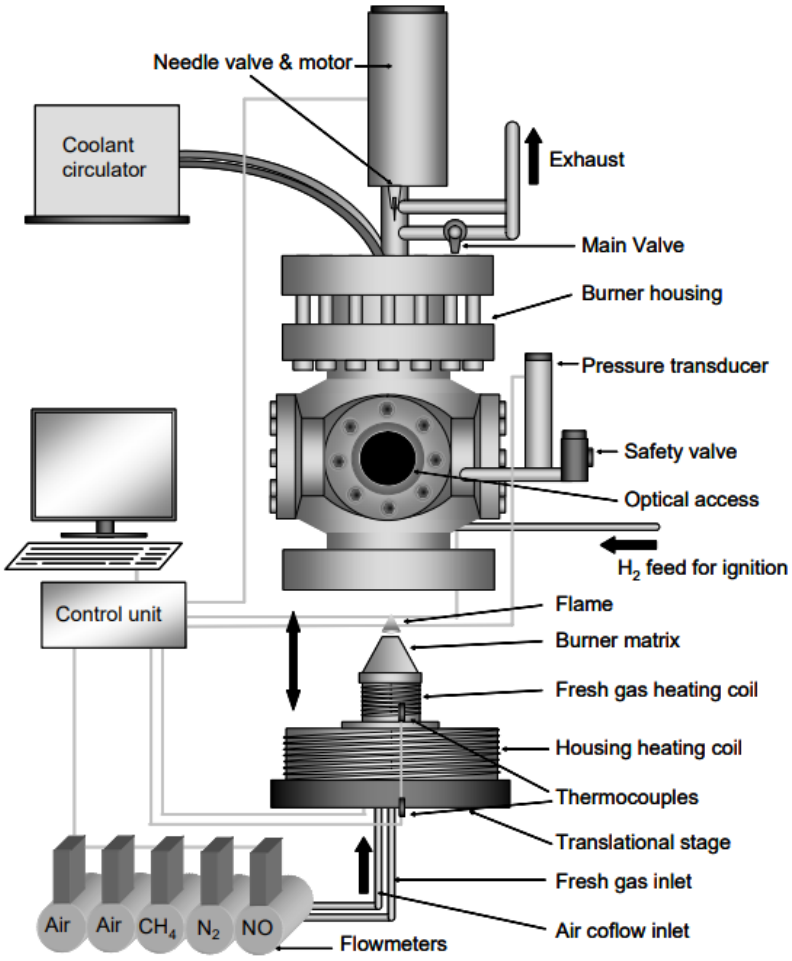

Fig. 2: Stanford Engineering Flow reprinted from [11]

Several other institutions have also used high-pressure burner facilities with a similar concept of operation. The DLR dual-swirl burner and the high-pressure facility in Germany [4,10] and the burner system from the combustion laboratory of l'Institut National des Sciences Appliquées de Rouen, which is shown in Fig. 3 below, are some examples. This burner is similar in operation to the Stanford burner, except that the burner can also operate on liquid fuel, and the pressure is regulated through the closing of sonic nozzles. In addition, the burner preheats the combustion reactants. A guard flow is used to adjust the pressure in the vessel and to dilute the gases coming from the exhaust. Similarities are seen with a stainless-steel combustion chamber with optical windows for laser diagnostics.

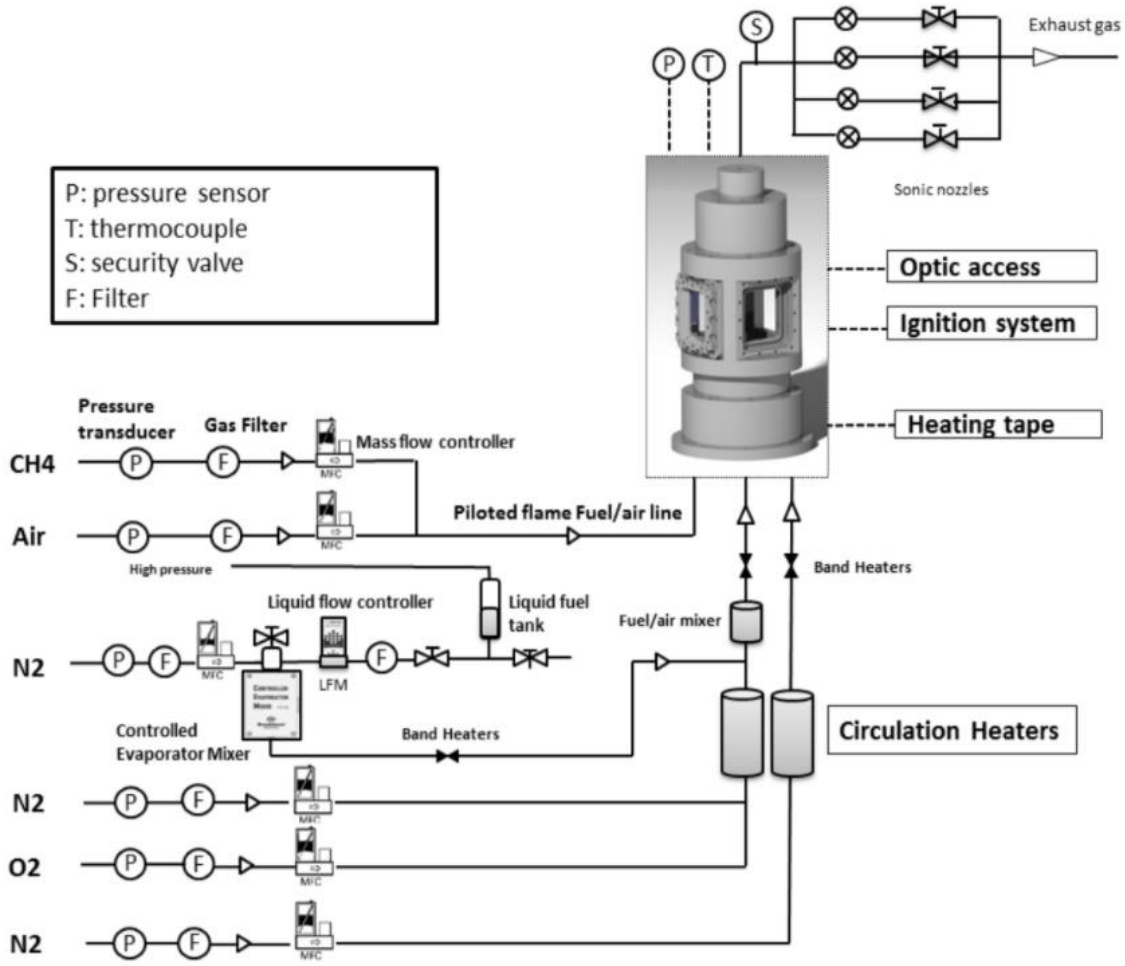

Fig. 3: Burner Facility Control Schematic reprinted from [12]

The ICARE-CNRS laboratory has also been conducting experiments with a high-pressure counterflow burner. This burner, as shown in Fig. 4, is in the counterflow configuration but still retains the same basic setup of optical windows for laser diagnostics, namely, a stainless steel hull to help with the high-pressure and temperature conditions and a pressure transducer and control valve to regulate the gas flow out of the burner.

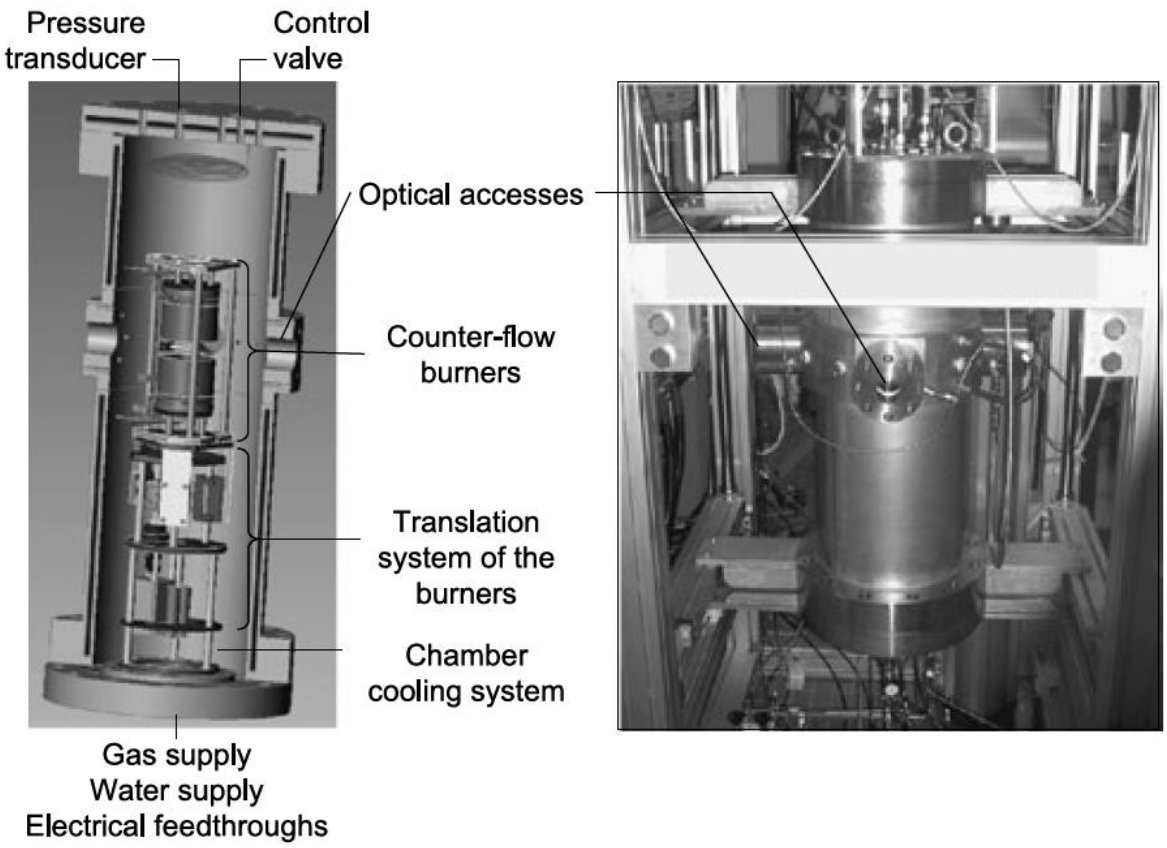

Fig. 4: The High Pressure Counterflow Chamber in Operation at the ICARE-CNRS Laboratory reprinted from [7]

Finally, The University of Duisburg-Essen has a well-established high-pressure burner system for soot measurements shown in Fig. 5. The burner is constructed from stainless steel with a large-bore area of 90 mm [13]. It is equipped with four quartz optical windows for laser diagnostics enabling ample access to the flame. Co-flow helps to stabilize the inner premixed flow, and pressure is regulated through a back control valve.

‘

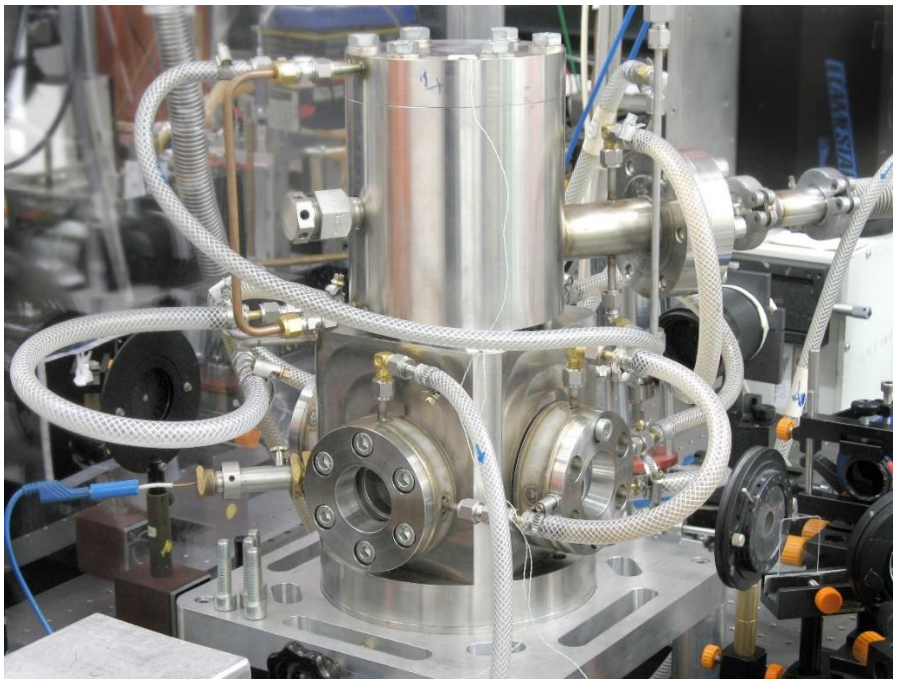

Fig. 5: High Pressure Burner Facility University of Duisburg-Essen reprinted from [13]

Thermal, mass flow, and pressure management, which are the key factors with all of these systems, were consistently prioritized in the construction and implementation of the TAMU high-pressure facility. Thermal systems included the thermocouples and water cooling lines routed throughout the burner. Mass flow control was similar to the Stanford system in that regulation was achieved through electronically regulated controllers. Pressure management was achieved through pressure transducer and control valve instrumentation. In the burner section of this thesis, these commonalities are further demonstrated through the corresponding engineering systems presented in the TAMU burner.

2.2 Chemiluminescence Diagnostics

2.2.1 Chemiluminescence Imaging Fundamentals

Chemiluminescence is defined as the light emitted as a result of a chemical reaction. During a combustion event, energy is added to the reactant molecules, which are broken apart and form new bonds and atoms, and at the same time, the atoms and molecules collide with one another [14]. In the intermediate reactions between the first and last step, molecules with an extra unpaired valence electron can be formed. These molecules are considered radicals and collide with other particles around them while absorbing some kinetic energy. This kinetic energy excites the unpaired electron and causes it to progress to an electronically higher energy state. Depending on the molecule being excited, a photon will be emitted at different wavelengths corresponding to the difference in energy between the excited and relaxed states of the molecule. This process is called chemiluminescence, and a sample image from a recent publication is shown below.

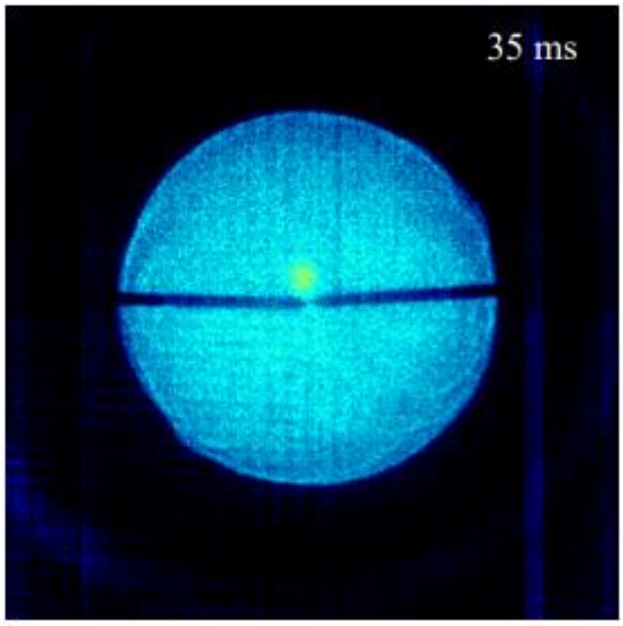

Fig. 6: High-speed chemiluminescence image of OH* in a spherically expanding flame reprinted from [14]

The light produced by this process can be captured by a camera using a bandpass filter centered at the specific wavelength associated with the electronic transitions. OH* at 315 nm and CH* at 434 nm are common radicals that are evaluated during this study, as they are known to be useful in characterizing reaction zones and flame oscillations in combustors [15, 16]. For combustion applications where scientists want an overall idea of the combustion regions, low-speed ICCD cameras have been used successfully. The disadvantage is that the cameras will output a single snapshot or a time-averaged image that does not completely represent the flame. Therefore, to fully investigate the flame instabilities and radical concentration, high-speed cameras are necessary to capture emissions in the order of kHz rates for a more accurate representation of the real-time combustion properties of the flame.

2.2.2 High-Speed Imaging for Combustion

High-speed imaging in combustion is an ongoing research area with the potential to provide significant clarity to combustion processes. The paper by Sick sums up the need for high-speed imaging "nonlinearities currently prevent us from understanding the evolution of a flame if we take snapshots at successive times that are too far apart, i.e., statistically uncorrelated." [17] Essentially, with lower rate cameras, the frames will be taken too far apart to provide an accurate portrayal of the flame motion as it creates a time-averaged effect [18, 19]. Hence, high-speed imaging is useful as it typically has a frame rate of 1 kHz and above. Previous works with high-speed imaging have been used for flame extinction studies and determining the lean blowout limit [20], flame propagation and growth rates, [21, 22], velocities and species concentrations [23, 24], and many other combustion parameters such as 3-D imaging of the combustion event [25]. In this study, flame stability was the driving factor behind the implementation of high-speed imaging. The OH* radical was targeted as in a previous study by Stojkovic [26]. While the CH* radical can serve as a flame front marker, and through proper post-processing, the OH* images can be used to determine the flame's stability based on the fluctuation of the signal strength in the target portions of the flame.

2.3 Hydroxyl Radical (OH) Planar Laser-Induced Fluorescence (PLIF) Imaging

2.3.1 Theory of Laser-Induced Fluorescence

Laser-induced fluorescence (LIF) is a spectroscopic technique that involves the excitation of a target molecule by a beam of laser radiation followed by detecting the subsequent emission of radiation [27]. A schematic of the energy level diagram of the LIF process is presented in Fig. 7.

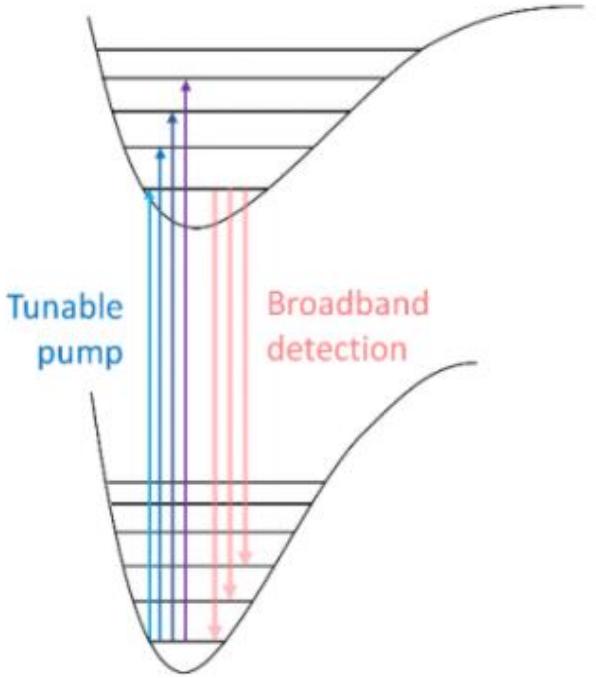

Fig. 7: Laser-Induced Fluorescence (LIF) Energy-Level Diagram reprinted from [28]

A tunable dye laser is typically set to a specific wavelength to excite molecules to the upper electronic states. As the molecules transition back from their upper states, a photon is emitted in the form of fluorescence. A camera or detector is then able to record this fluorescence signal. These images produce a picture of where chemical species associated with the excitation wavelength exist in the combustion zone because only the molecules that were excited by the wavelength from the laser will fluoresce. The paper by Grisch et al. explains the theory behind the LIF in considerable detail [29].

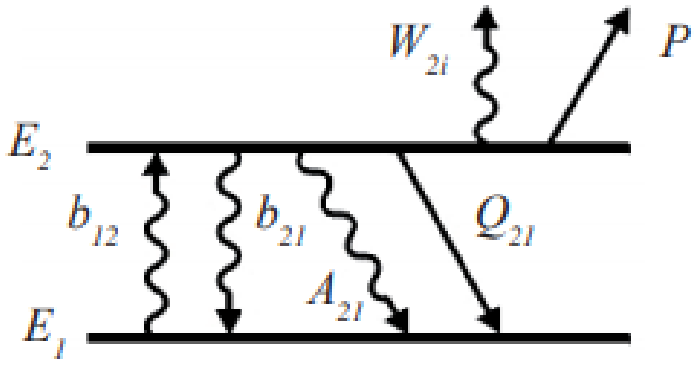

Fig. 8: Two level Fluorescence Model reprinted from [29]

The two-level model shown in Fig. 8 explains the energy transitions between the upper and lower levels during LIF. E_1 is the upper energy level, and E_2 is the lower energy level. $b_{21}$is the stimulated emission, and b_{12} is the absorption. A_{21} corresponds to the rate constant for the emission, which can be considered as the fluorescence signal. W_{2i} is the photoionization, and P is predissociation. Q_{21} is the collisional quenching or signal loss of the fluorescence, which corresponds is given below:

$$Q_{21} = N \sum_i \chi_i \sigma_i v_i \qquad (1)$$

χ_i is the collider mole fraction of the species, σ_i collision cross-section, v_i is the mean molecular speed between the colliding and absorbing species. The rate equations for the population densities of the energy levels help relate the constants to the total number of photons emitted. The rate equations are quantified below, with N_1 and N_2 being the population densities of the two separate energy levels.

$$\frac{dN_1}{dt} = -N_1 b_{12} + N_2(b_{21} + A_{21} + Q_{21}) \qquad (2)$$

$$\frac{dN_2}{dt} = N_1 b_{12} - N_2(b_{21} + A_{21} + Q_{21}) \qquad (3)$$

After several manupulation steps documented in the paper, including relations for saturation irradiance and initial conditions, an expression is derived for the total number of photons N_p detected by a photodetector, as,

$$N_p = \eta \frac{\Omega}{4\pi} f_1(T) \chi_m n V B_{12} E_v \frac{A_{21}}{A_{21}+Q_{21}} \qquad (4)$$

n is the transmission efficiency for collection optics, Ω is the solid angle of collection, and the term $f_1(T)$ relates to the fractional population of the lower-coupled state. χ_m is the fraction of moles in the absorbing state, n is the total gas number density, E_v the spectral fluence of the laser, and the term $\frac{A_{21}}{A_{21}+Q_{21}}$ is referred to as the Stern-Volmer factor for the fluorescence yield. Quenching rates are also considered to ensure that the measurements are taken in the linear region where the LIF signal is proportional to the number density of the targeted molecule. LIF has been a vital diagnostic tool employed in combustion experiments since it was conceived by Zare in 1968 [27]. The technique has been used to study flames extensively because of its ability to detect the concentration of different chemical species nonintrusively [30–32]. The main disadvantage of this technique is that it is only sufficient to provide accurate species concentration at a particular point in the combustion flame. Planar laser-induced fluorescence (PLIF) uses the same concepts as LIF, but it produces a laser sheet to offer a 2-D view of the combustion event. This technique has the potential to produce not only species concentrations as in LIF but also temperature, pressure, and velocity measurements of the combustion event. [33].

2.3.2 OH PLIF

Typical species investigated in PLIF studies include OH, CH, NO, and different tracers in the combustion events [34, 35]. The current study focuses on the species concentration of the well-documented hydroxyl radical [35–39], which has also been proven to be a combustion zone marker, which allows an accurate view of how the combustion process is evolving with changing equivalence ratio and pressure. Shown in Fig. 9 is a typical image of an OH PLIF flame.

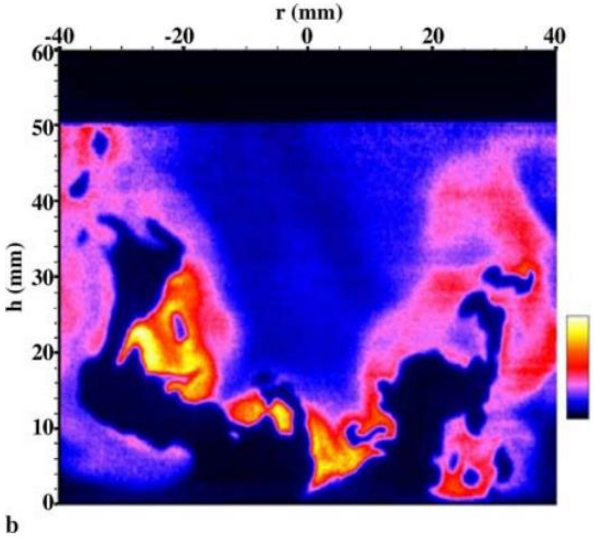

Fig. 9: OH PLIF Image from a Gas Turbine Combustor reprinted from [40]

These results highlight the importance of the OH PLIF measurements. Chemiluminescence measurements or point detectors would not yield the same level of information as described above. An outside observer might conclude that the flame is more symmetrical than it really is or that the combustion front is distributed symmetrically across the entirety of the flame. As depicted above, the OH PLIF measurements tend to reveal a different representation regarding the disruption of the combustion flame front. As such, these measurements are critically important for combustion research as they can help engineers and scientists design and validate more efficient combustion systems.

2.3.3 Spectral Line Selection

Typical excitation schemes of the OH radical usually involve targeting the $A^2\Sigma^+ \leftarrow X^2\prod$ (1, 0) band of the OH radical, followed by fluorescence detection from the A←X (1, 1) & (0,0) bands. Numerous factors are considered when selecting a wavelength, including absorption effects, the laser that will perform the excitation, and the electronic energy levels of the excitation and emission bands of the molecule. In a recent work by Boxx et al. [10], the $Q_1(7)$ rotational line was targeted for high-pressure combustion work owing to its documented low-temperature dependence and strong fluorescence output at the excitation wavelength of 283.305 nm [35]. LIFBASE simulations shown in Fig. 10 were performed at different pressures to determine if the line selection was accurate. The simulations produced similar results to those outlined previously in the literature. Collisional, Doppler, and pressure broadening were all accounted for in the model. The area underneath the peak location of 283.305 nm line increased significantly with pressure. This result was expected due to the pressure broadening effects. With an increase in pressure, collisional broadening dominates and causes the spectrum to become wider [35]. Overall, the $Q_1(7)$ rotational line was a suitable choice for high-pressure combustion conditions.

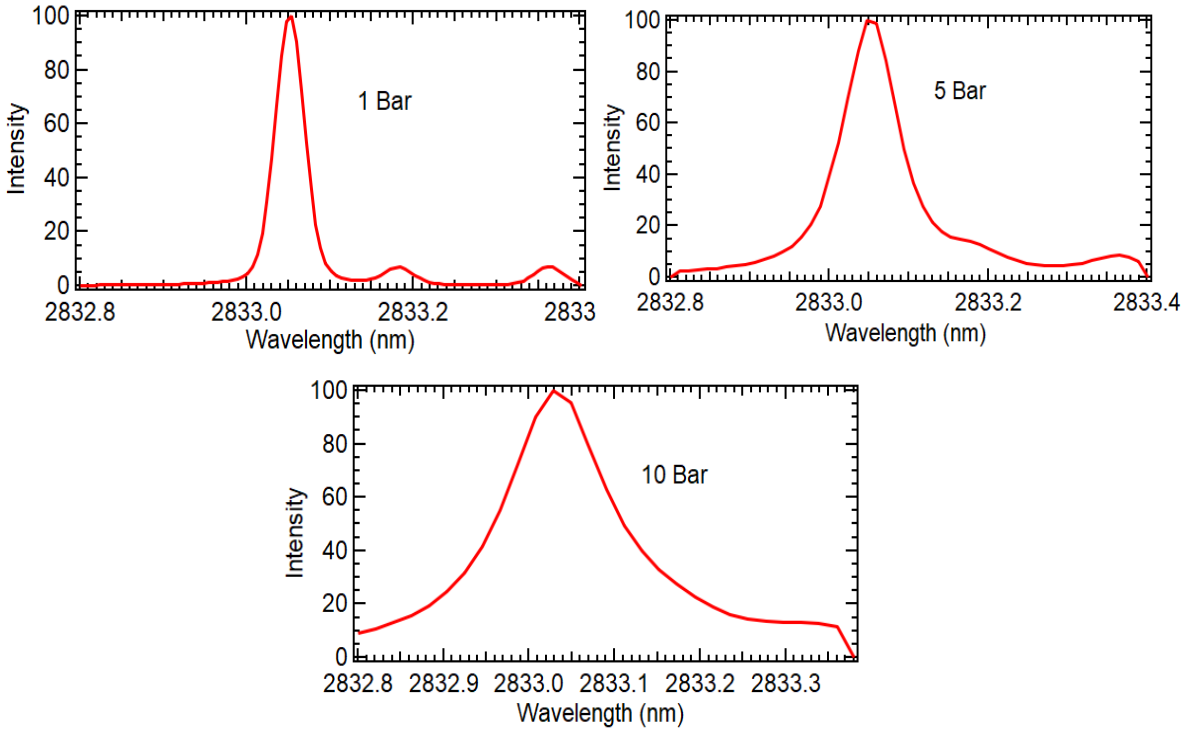

Fig. 10: LIFBASE simulations (1,5 and 10 Bar)

2.3.4 Quenching Correction

One of the major interferences responsible for the disparity during OH-PLIF measurements at higher pressures is collisional quenching effects. Most studies have experimentally determined quenching rates under atmospheric-pressure conditions while calculating the quenching rates based on quenching cross-sections and concentrations of major colliders at higher pressures. The major species in most of these works are CH_4, H_2O, CO_2, O_2, H_2, and CO in premixed CH_4/air flames. The corresponding temperature- and pressure-dependent cross-sections in this work were determined based on a "harpooned model" proposed by Paul [41]. The term is coined because upon transfer of an electron, the strong charge--charge forces between the ions bring the collision partners to close proximity [41]. In this model, the coefficient for the quenching of OH by N_2 is zero, and thus there is little contribution to collisional quenching of OH-PLIF signals. The

application of this model is important because of the significant loss of signal seen in conventional OH-PLIF experiments at higher pressures [42]. The calculated quenching rates for this study are shown below in Fig. 11.

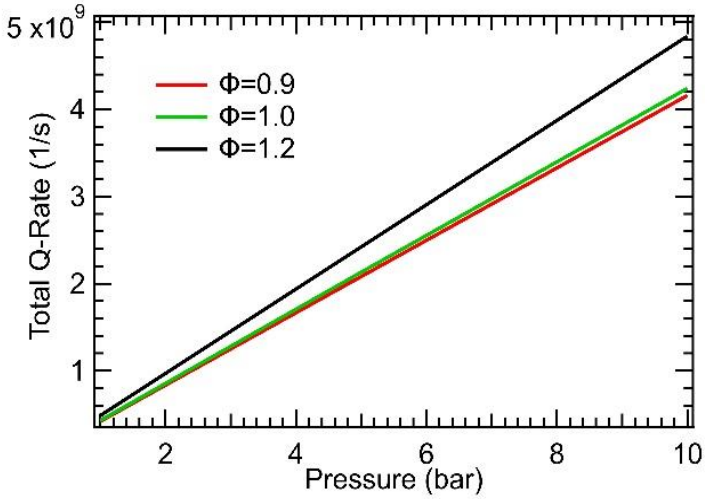

Fig. 11: Graphical representation of quenching rates

These rates are extremely important for post-processing, as the typical losses of signal from 1–10 bar can be as much as 80%, as demonstrated in Fig. 12.

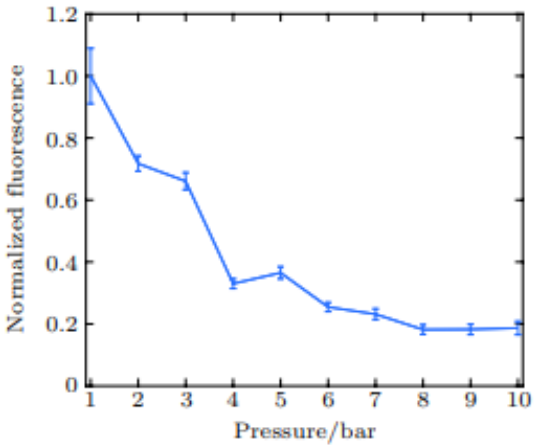

Fig. 12: Fluorescence as a function of pressure for the Q1(8) wavelength of OH Radical reprinted from [42]

This phenomenon helps to explain why studies of radicals at higher pressures are challenging and why the literature has fallen short of creating an excitation scheme to eliminate the effects of quenching. These observations lead to a discussion of high-pressure OH PLIF diagnostics and recent advances in laser technology that are improving the experimental results from these signals.

2.3.5 High-Pressure OH PLIF

Most OH-PLIF experiments reported in the literature have been conducted at lower pressures [43–45]. Conducting OH-PLIF at higher pressures, however, adds significant complexity. The OH PLIF mechanism involves two main stages: the first being the molecule absorbing the laser energy and reaching a higher energy state. The second is the relaxation of that molecule. Pressure broadening is the primary interference that will occur in the first stage as the targeted linewidth of the excitation will become significantly broader due to pressure effects, as seen in the wavelength selection section in work by Singla [35]. Doppler effects can also shift the location of the excitation spectrum, as noted before, but this was not found to be a significant factor for the current study.

Quenching effects, as discussed, are the main issue at the second phase for high-pressure experiments and the underlying reason why accurate LIF measurements are challenging to obtain at high pressures. Collisional quenching is the dominant interference mechanism when transitioning into high pressures, as noted by Atakan [4]. The basic premise is that when the molecules are excited to the upper state, some of the energy does not release itself in the form of light emission. The excited molecules collide with other molecules and release the energy instead of being released through fluorescence as the molecule relaxes. The pressure increase guarantees that the molecules will be closer together and move more quickly; therefore, collisional quenching will increase significantly at higher pressures. As a result, the fluorescence signal will be

substantially weaker at elevated pressures, even though the signal should theoretically be increased to reflect the increase in the number density of the OH radical.

Other energy transfer processes, including rotational and vibrational energy transfer, need to be quantified and accounted for as correctional factors. The studies conducted by the Chinese Scramjet Laboratory and by Purdue University [10], and German DLR [46], have all encountered similar issues. Shown in Fig. 13 is an OH PLIF image taken from the paper by Boxx [10]. The brighter parts of the image correspond to the OH-PLIF concentrations in the combustor. Laser sheet absorption was apparent as the left and right sides of the signal had significant variations. The low signal-to-noise ratio results from the interferences mentioned before and is one of the main difficulties faced by combustion researchers.

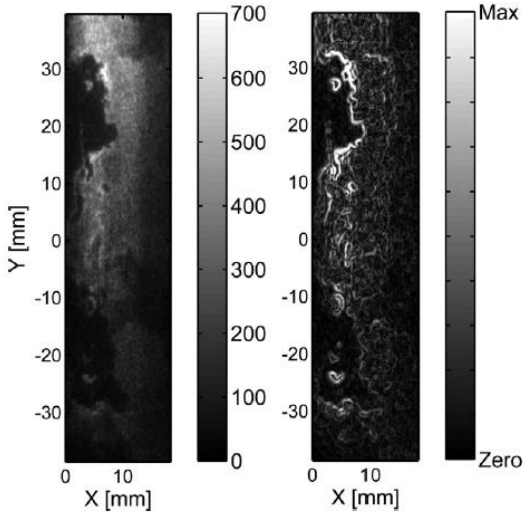

Fig. 13: High Pressure OH PLIF Measurement at 5 bar reprinted from [10]

3. DEVELOPMENT OF TAMU EXPERIMENTAL HIGH-PRESSURE BURNER FACILITY

3.1 General Burner Construction

3.1.1 High-Pressure Vessel

As mentioned before, high-pressure burners are a unique and valuable tool for simulating realistic combustion scenarios for laser diagnostic studies. The physical components of the burner are discussed under two sections: a high-pressure vessel and a burner with a translation system. The high-pressure vessel is shown in Fig. 14, along with the window holders and quartz windows.

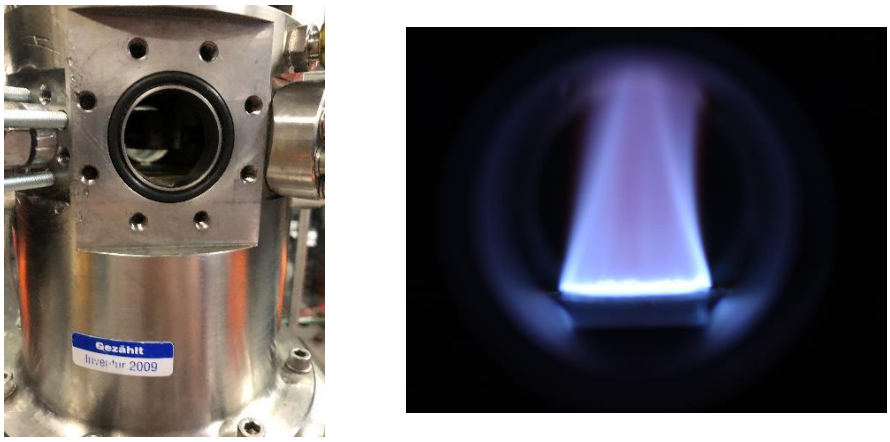

Fig. 14: High-Pressure Burner Vessel (**Right**), Methane/Air Flame at Φ=1.2 and 4 bar **(Left)**

The stainless-steel hull is manufactured from 316 stainless steel, which can withstand the 50 bar designed operating pressure of the burner. The mechanical properties of stainless steel allow for significant thermal and pressure-induced stresses without the possibility of failure during experiments. The fused silica optical windows are seen above in the window holder on the burner. The optical windows were vital for providing optical access to the flame to perform follow-on laser diagnostics. The challenge was to design an optical window system that would allow for sufficient mechanical as well as optical characteristics. Materials for 'Infrared Windows and Domes, Properties, and Performance' [47] provides some useful equations and documentation on

the design of the pressure constraints. Equation (5) below from the book was used to determine the minimum thickness needed to withstand the pressure forces.

$$t_w = .5 * \emptyset_a \sqrt{[K_w * f_s * \frac{\Delta P}{\sigma_{YS}}]} \quad (5)$$

The calculation was conducted considering both sapphire and fused silica, which are the most common optical materials used in high-pressure conditions. The team opted to use fused silica because of the sufficient optical and mechanical characteristics of the windows at a relatively low cost.

3.1.2 Burner and Translation System

The flat flame burner and translation system are the second set of physical components needed for the operation of the facility. The burner consists of two rings, both of which are made of sintered bronze that are porous in nature. The bronze is of B20 quality with porosity ranging from 34–39%. This component acts essentially as a flow straightener and a filter to allow uniform combustion of the air and fuel mixture. Fig. 15 shows the inner and outer rings of the burner surface. The inner ring flows a methane and air mixture that is ignited in the burner's combustion chamber. This ring is 20 mm in diameter and is fed through the bottom of the burner by a mass flow delivery system. The flame is considered premixed as the air and methane are mixed before propagating to the top of the surface. The outer ring is 40 mm in diameter and is used as a co-flow ring for the system. This co-flow is comprised of air and acts as a flow straightener for the premixed flame. The outside air coming from the second ring helps shield the inner ring from inconsistencies in flow caused by the high-pressure environment inside the burner. Finally, the small holes on the exterior of the stainless-steel burner shell are the nitrogen guard flow for the system. The nitrogen guard flow provides another inlet for gas to serve two main functions, adding

more gas to pressurize the system further and help convectively cool the vessel and windows. A simplified flow diagram is presented in Fig. 16:

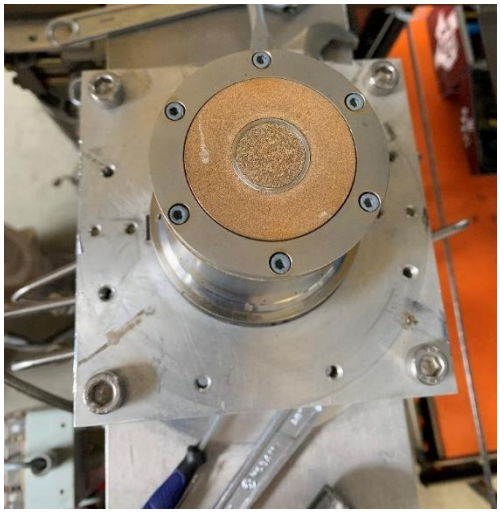

Figure 15: Flat Flame Burner

The sintered bronze flat flame apparatus is often used in conventional combustion experiments at atmospheric pressure. However, the difference here is the stainless steel shell that is placed over the burner and sealed with O-rings to allow for pressurization. This feature allows for pressure control over the system and the ability to reach higher pressure environments. Shown in Fig. 17 is a cutaway view of the stainless-steel hull and burner generated using SOLIDWORKS, which shows the inside features of the stainless-steel hull and the burner.

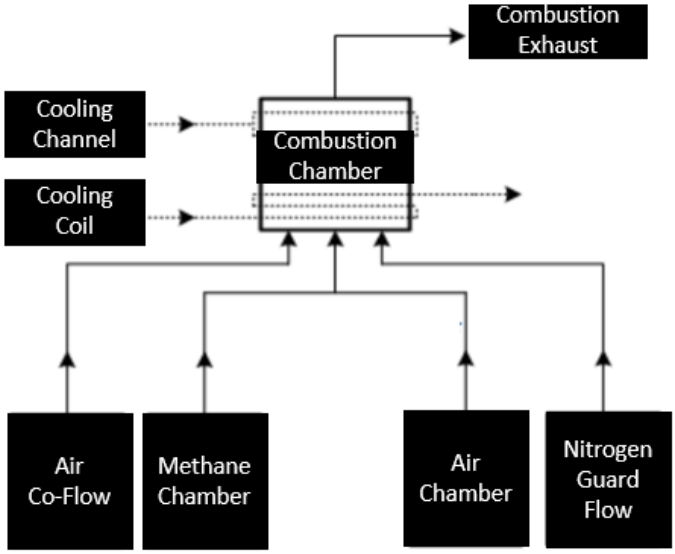

Fig. 16: Simplified Mass Flow Schematic

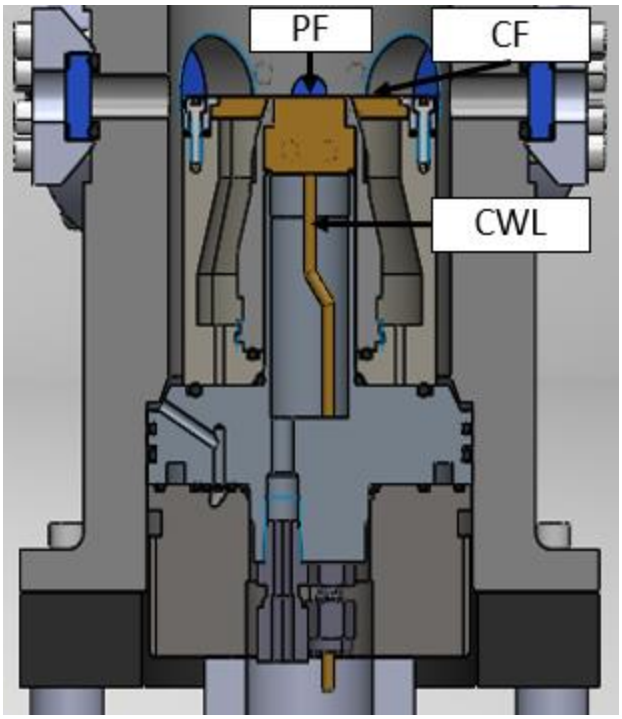

Fig. 17: Cutaway of the Burner Assembly; PF=Premixed Flow, CF=Co-Flow, CWL=Cooling Water Line

The basic concept behind bringing the system to high pressure is as follows. Gases are pushed into the system using the three gas pathways mentioned earlier. The flow rate determines the amount of pressure inside the system at any given time. If more flow is put into the system, the pressure increases accordingly, as defined by an ideal gas law relationship corrected for pressure and temperature assumptions. Finally, the exhaust valve at the outlet can also influence the pressure based on the size of the diaphragm opening determined by the setpoint in LabVIEW controls discussed below.

Fig. 18: Burner Vertical Translation Mechanism

In order to achieve optical access, the translation mechanism adjusted the height and sightline of the flat flame burner vertically relative to the fixed height of the pressure vessel mounting frame, as shown in Fig. 18. The mechanical components of the high-pressure burner facility consisted of a stainless-steel hull, optical windows, and a flat flame burner encased inside the shell. Each component played a role in ensuring the safety and stability of the high-pressure facility. The

following sections will discuss the systems that made the operation of the burner possible. A fully assembled burner facility is shown in Fig. 19.

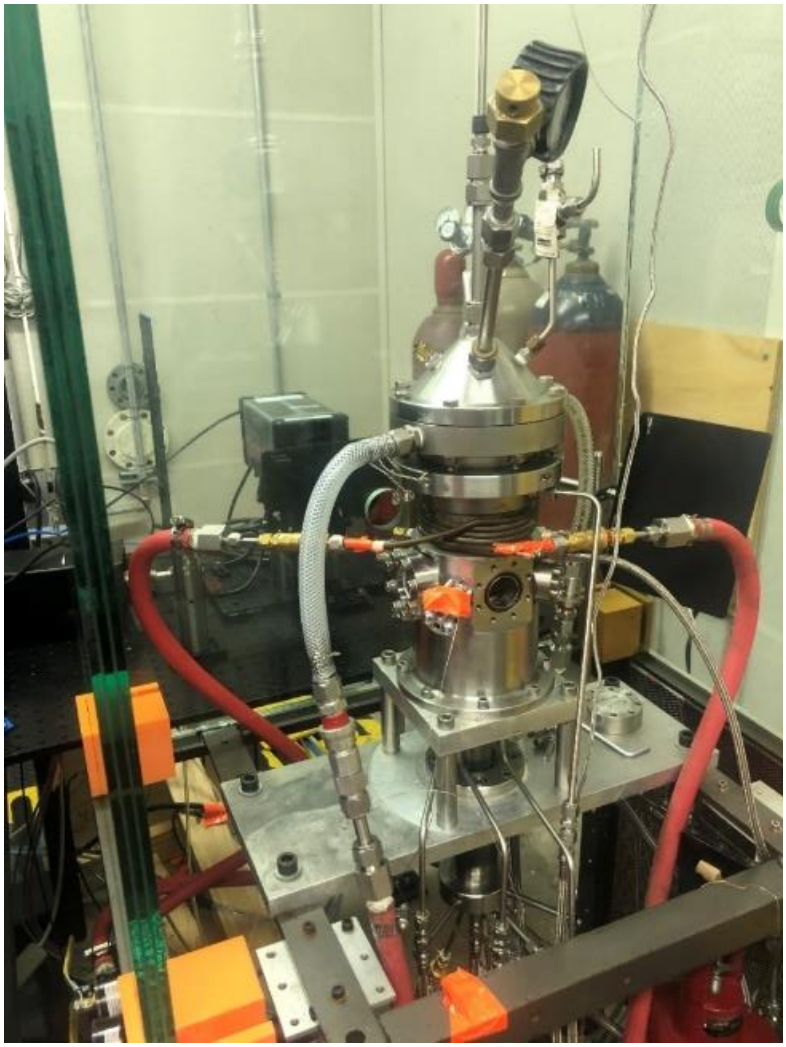

Fig. 19: Fully Assembled High-Pressure Burner Facility

3.2 Gas Flow System

3.2.1 Mass Flow Calculations

As stated previously, the high-pressure burner facility consisted of three inlet gas flows, a methane and air premixed flow, an air co-flow, and a nitrogen guard flow. The challenge was to optimize the flow rates of these gases into the burner in order to obtain the desired equivalence ratio for the flame and the desired stable target pressure. The pressures targeted for this study were 1–10 bar, and it was determined that at these pressures, an approximation of the ideal gas law was acceptable because the temperature was sufficiently high, and the pressure remained above the critical pressure for air and methane.

The main goal was to create a stable flame at all pressures. It was experimentally determined that the lower pressures needed a higher inlet velocity from the premixed gases for increased stability. As the pressure increased, the stability of the flame increased with lower inlet velocities. The inlet velocities varied from 14 cm/s to 6 cm/s with 14 cm/s corresponding to 1 bar and 6 cm/s, corresponding to 10 bar. The desired velocity was then multiplied by the area of the premixed surface to obtain a volumetric flow rate for the air and methane mixture. Pressure and temperature increases were accounted for using factors derived from the ideal gas law. The two flow rates were then corrected for error using REFPROP software [48], which predicted the densities of the gases according to the conditions used in our laboratory. The co-flow and nitrogen guard flow were calculated using the same method of scaling the flow rates with pressure and kept at a fixed rate of 6 cm/s, which was found to be the most stable for the application. The spreadsheet is documented in the Appendix used for these calculations.

3.2.2 Mass Flow Controllers

After the calculations for the mass flow rates were derived, suitable mass flow controllers needed to be implemented into the system. For inial studies, high-pressure manual rotameters were used as a suitable replacement for an expensive mass-flow controller system. The Matheson 1050 FM rotameters selected are displayed in Fig. 20.

Fig. 20: Matheson Flow Meters reprinted from [49]

Rotameters consist of a glass tube containing one to two floats based on the flow rate entering the tube will oscillate either up or down. Rotameters are inherently less precise than electronically actuated mass flow controllers. However, the accuracy was determined to be acceptable because of the low flow rate of the premixed methane and air mixture. The selected rotameter accuracy is 5% of the full scale for all measurements. For the co-flow and nitrogen guard flow, 5% accuracy was acceptable because it would not significantly impact the results if the pressure could be kept

constant with the electronic control system. However, for the premixed flow, a variation of 5% would lead to higher inaccuracy than is experimentally acceptable. Rotameter calibration was obtained from the manufacturer so that at 15 bar, the flow accuracy increased to 1% of the full scale. Calibration curves were provided by Matheson, which showed the relationship between the volumetric flow rate and meter reading of the balls inside the tube that indicate the meter reading. The meter readings from Matheson were mathematically modeled using an excel sheet so that a program could be created to simulate the mass flow rates needed for each step. The spreadsheet in the Appendix outlines the conversion from the desired mass flow rates into the meter reading of the actual position of the floats within the tube.

After experimentation, it was determined that the rotameters for the premixed portion of the control would not be viable for regulating the mass flow rates in a way that would provide meaningful data. The details of these experiments are outlined in the section discussing the stability of the chemiluminescence. The electronic mass flow controllers selected in their place were MKS flow controllers. The flow rates for these controllers were regulated using the Model 946 controller system from MKS. Overall, the controllers showed improvement in flame stability as well as the accuracy of the flow rates into the burner.

3.2.3 Gas Plumbing System

The mass flow controllers facilitated the regulation of the gases into the high-pressure burner facility. However, each of these mass flow control loops had a different piping system to enter the burner. In this experimental setup, all the gases were supplied in gas bottles. All gases had pressure regulators attached to provide an inlet pressure control. A 6-mm flexible tubing was attached to the pressure regulators and routed to the mass flow controllers. An overview of the entire system from the tank to the high-pressure facility is displayed in Fig. 21.

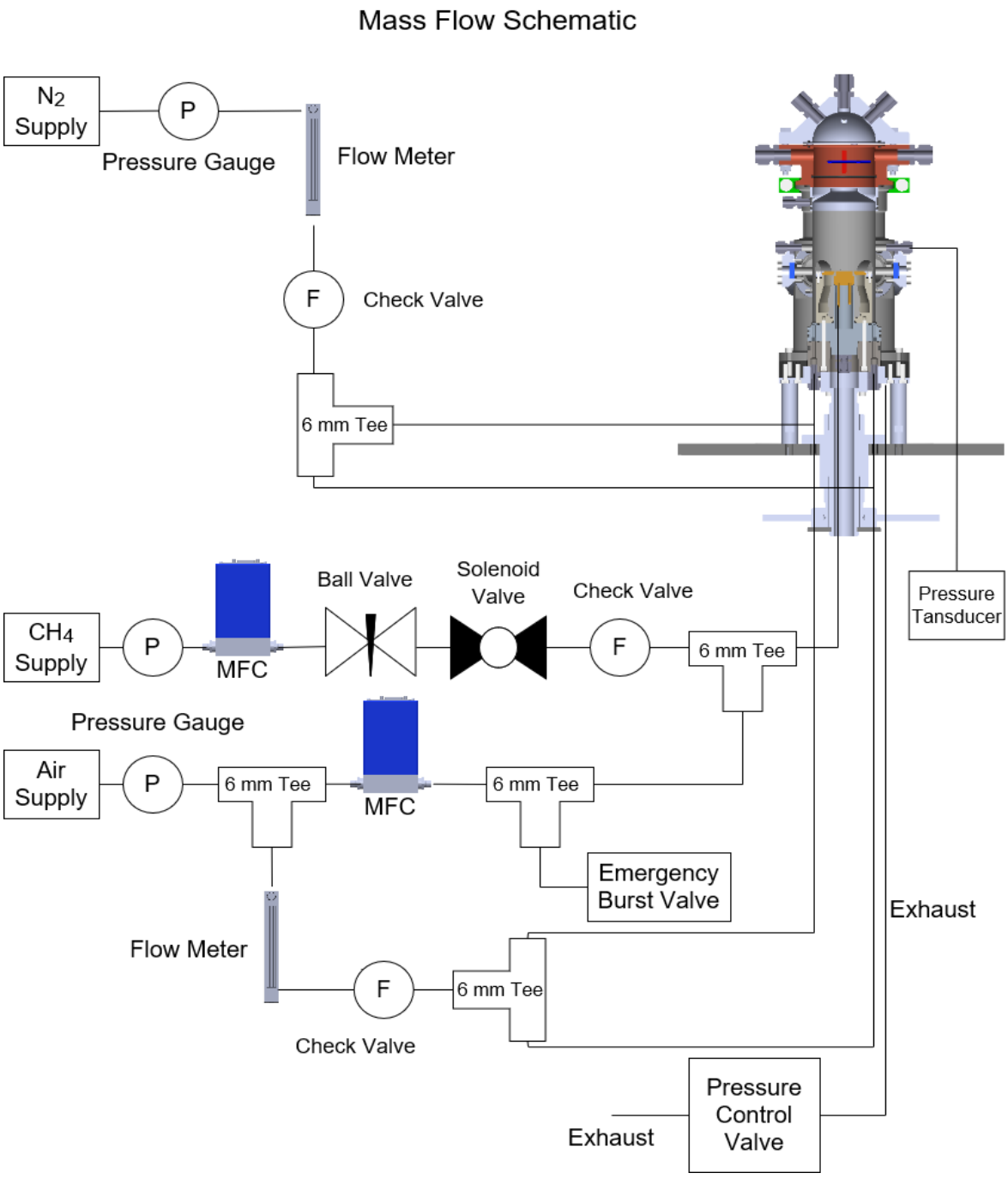

Fig. 21: Mass Flow Schematic

The co-flow and guard flow systems were both routed using the Matheson mass flow controllers into a Swagelock 6-mm T-connection. The burner facility had two inlets for the guard flow and co-flow to allow for a more symmetrical distribution of the flow. Therefore, the T-

connection allowed for consistent flow from the guard flow and co-flow into each inlet from the same supply source. The premixed flow system was responsible for the actual combustion of the flame, and therefore, more components were necessary to ensure safe operation. The system consisted of a methane side and an airside. The airside passed from the mass flow controller into a T-connection in the middle section of the facility. One side of the T-connection continued into the facility with the purpose of premixing with methane.

The other side had a burst disc from McMaster-Carr attached to the other side. If a pressure buildup should occur from failure of the burner actuation system, pressure regulator, or the lines themselves, the pressure needed to be relieved somewhere safely. It was decided that the discharge of air alone would be much safer than a discharge of methane into the air, and the outlet was kept pointing towards the floor at the bottom of the system so that no one operating the burner would be harmed. The methane side of the system had four main components before the T-connection split off into the facility. The first was the backward propagation filter purchased from Swagelok, which is essentially a flow filter. In the case of a combustion event in the piping, it prevents back propagation of the explosion into the methane supply tank. The second and third components were both flow shutoff valves. First in line is a manual valve in which, in extreme emergencies, can be turned off by hand. The second is an electronic control valve that is connected to LabVIEW, which can be operated remotely. Many of the inlets and outlets from the lines were connected to each other, as mentioned above, by 6 mm plastic tubing that can withstand a pressure of 17 bar. Some of the connections also consisted of 6 mm stainless steel tubing, which in the future must be used to completely replace the plastic tubing in order to reach higher pressures, which will be expanded upon in future work.

3.3 Cooling System

3.3.1 Cooling System Design

The combustion event occurring in the vessel naturally generated a significant amount of heat. The heat output was sufficient to justify the design of a cooling system to ensure that the stainless-steel pressure vessel and other components attached would stay at a safe operating temperature. Fig. 22 below illustrates the water plumbing schematic of the burner system.

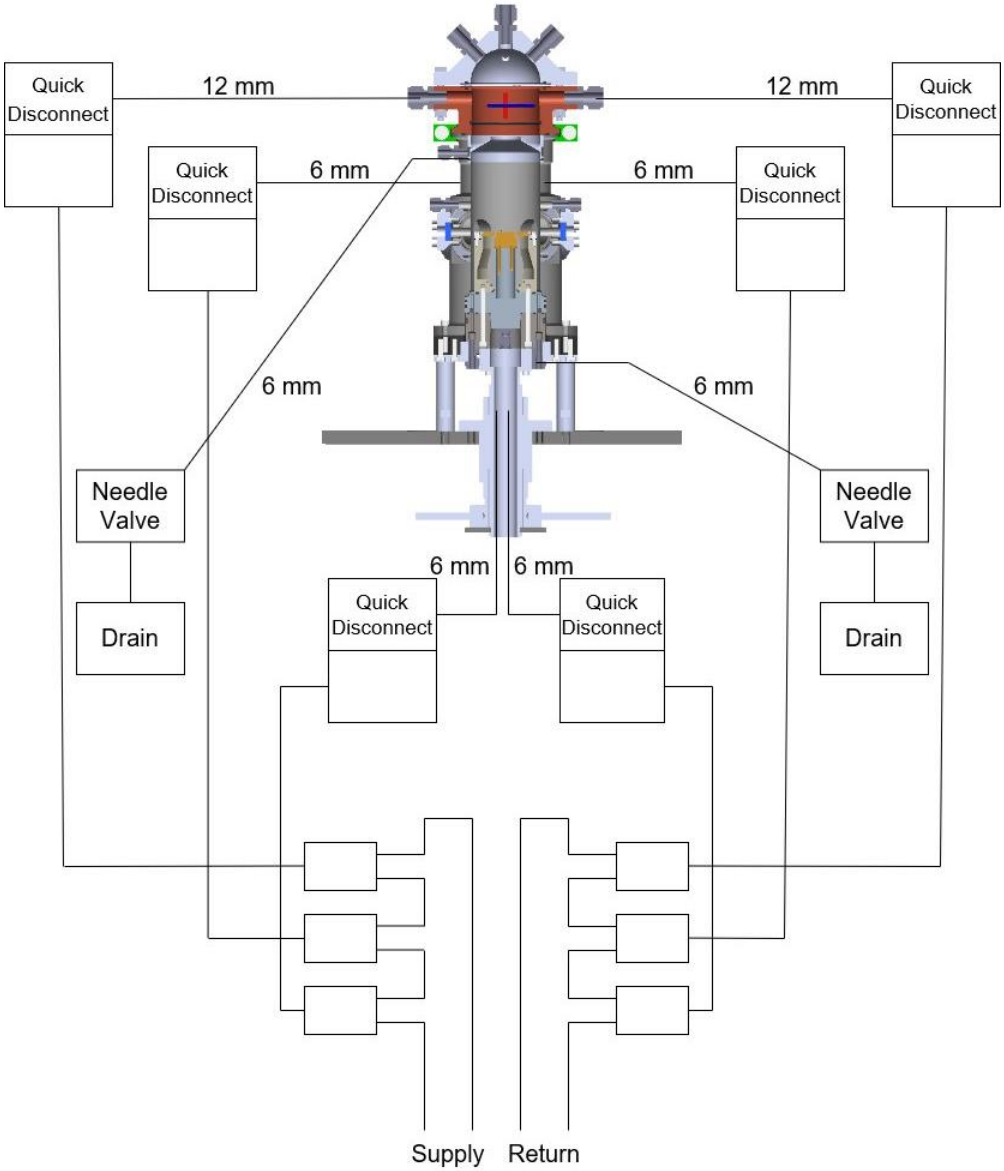

Fig. 22: Water Plumbing Diagram

As shown above, the system consisted of three inlets and outlets that were connected to different components of the burner. The system was fed by a pump connected to a 50-gallon water tank. The water then circulated through the supply to three different locations, a cooling channel, a cooling coil, and the burner internals diagrammed earlier. A picture of the three locations is shown in the simplified cooling diagram in Fig. 23, along with a model of the cooling coil and channel in reference to the stainless-steel body of the burner.

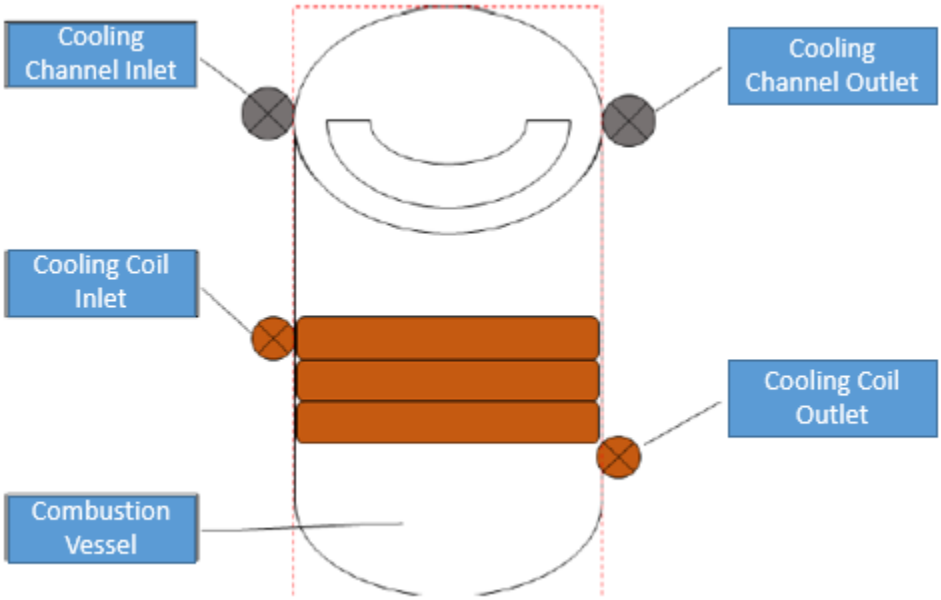

Fig. 23: Simplified Cooling Diagram

3.3.2 Cooling System Components

The cooling channel provided cooling through two 12-mm diameter holes cut into the top of the vessel "hat." This channel was determined to be one of the most effective areas for cooling the burner due to convective cooling from the guard and co-flow pushing the heat to the top of the vessel. The cooling coil was a 6-mm diameter copper tubing wrapped around the center of the pressure vessel and helped eliminate heat from the mid-section. Finally, two copper tubes circulate inside the flat flame burner as described above. The tubes maintain low internal temperatures in the bronze and stainless-steel components to ensure safe operation. Thermocouple data validated that the cooling system was effective in keeping the temperatures at a safe level, and the validity of the system is explained in the next section.

The water-cooling system consisted of three main components used for instrumentation, a water pump, a storage tank, and a cooling manifold. The water pump was capable of outputting a continuous stream of water at a rate of 6 gpm into the burner system. The pump itself was cooled by an exterior fan, but it did not overheat throughout the duration of the experiment. The storage tank was a 50-gallon tank with a specially fitted inlet and outlet flanges to ensure no leaks in the water system. The pump was directly connected to this tank with a straight pipe and then outputted to the cooling manifold. The cooling manifold consisted of brass T-connections, shutoff valves, and a water filter on the inlet side. The shutoff valves provided quick access for stopping the system in the case of an unexpected leak. Quick disconnect attachments were used for the cooling manifold as well as parts of the water pump and tank to ensure that the system could be broken down and transported as smaller parts. Red hoses attached to the manifold were high-temperature hoses capable of withstanding temperatures up to 300 °F and pressures in excess of 300 psi. Some key components of the flow system are shown in the pictures in Fig. 24.

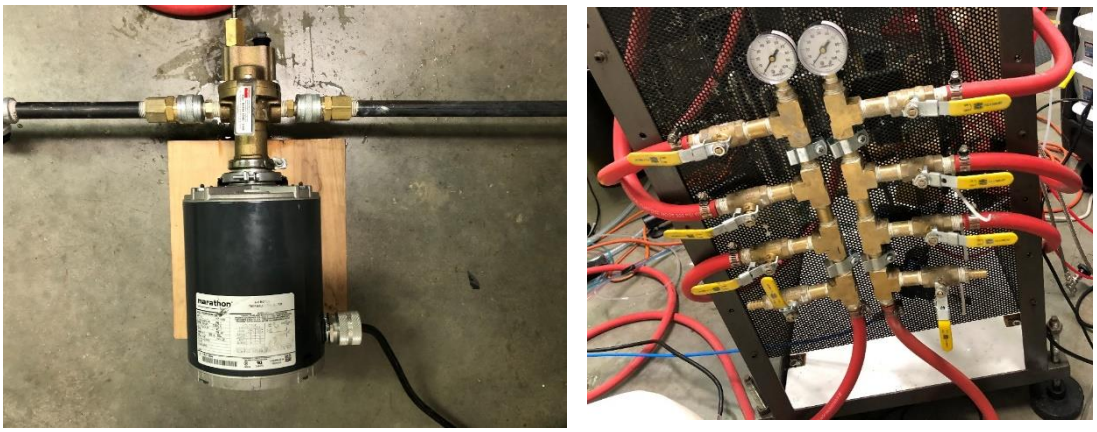

Fig. 24: Water Pump (Left), Water Manifold (Right)

3.4 Control System

3.4.1 Control Instrumentation

The high-pressure burner facility produced premixed flames using the physical components outlined in the previous sections. However, in addition to material and component selection for the physical elements of the operation, the controls, and electronic elements were vital to the operation. Three main goals had to be met in order for the facility to function safely and effectively, pressure, temperature, and fuel regulation. The control system must handle all three components from a remote computer so that the researchers could control the system from a safe distance. The schematic shown in Fig. 25 was designed and incorporated into the pressure and fuel regulation systems. Temperature regulation is in the subsequent section.

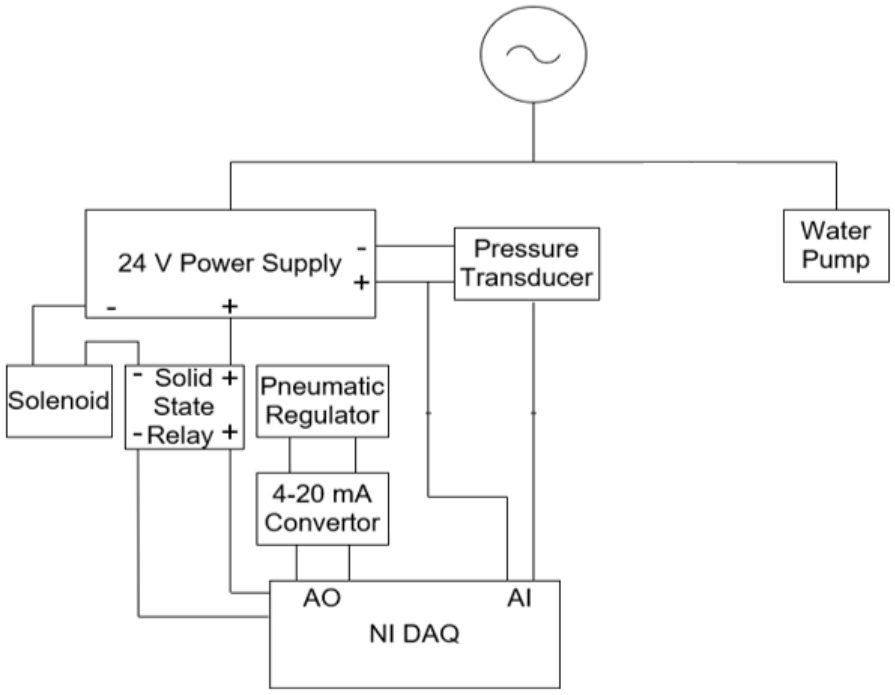

Fig. 25: Wiring Diagram

The final concept consisted of a pressure regulation system that implemented a PID loop to control the pressure and a solid-state relay connected to a solenoid to act as an emergency fuel shut-off switch. The fuel shut-off system was a relatively simple but valuable safeguard. A solid-state relay was connected to a 24 V power supply on one side and a National Instruments (NI) DAQ on the adjacent side. The relay was then connected to a solenoid that was directly connected to the fuel line. The purpose of the solid-state relay was to operate as an electronic on and off switch between the solenoid and the user on the computer. The NI DAQ system using LabVIEW "opened" the solid-state relay using a 5 V signal. This operation, in turn, allowed the 24 V power supply voltage to open the solenoid directly connected to the fuel line. By linking these two processes together, the user was able to instantaneously shut down the combustion of the flame in the case of an undesirable event.

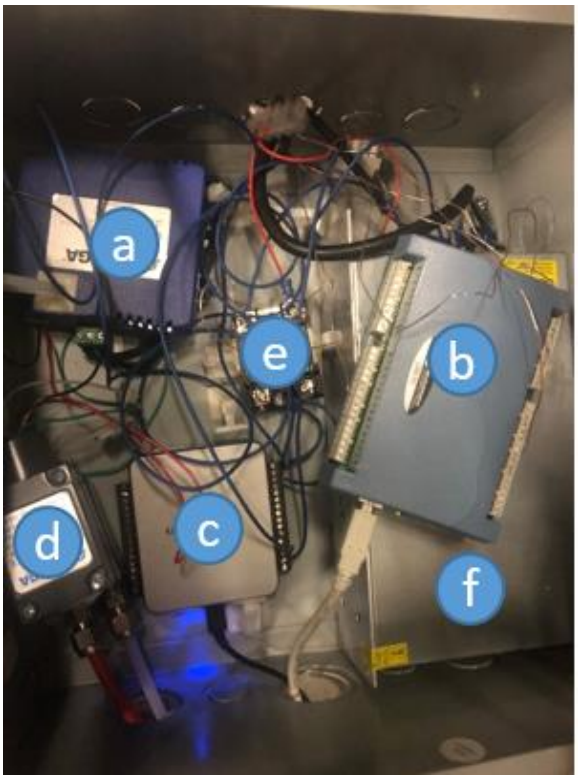

Fig 26: Control Box; A) Current Converter, B) Temperature DAQ, C) NI DAQ, D) Pneumatic Regulator, E) Solid State Relay, F) 24 VDC Power Supply

Pressure regulation occurs by implementing a PID loop in LabVIEW in tandem with a pneumatic pressure regulator, pressure transducer, and control valve. The Omega pressure transducer is connected to the body of the combustion vessel through a stainless-steel hose. The transducer sends a voltage signal of 0–5 V to the NI DAQ system, which converts the voltage into a pressure reading. This pressure reading is fed into the PID loop on the DAQ, which uses a setpoint controlled by the user, sends a voltage signal into the 4–20 mA converter. The 4–20 mA converter converts the voltage signal from the DAQ into a current that is fed into the pneumatic regulator. Based on the current received, the regulator would shift between 3–15 psi output pressure of air to the exhaust valve, which corresponded to the minimum and maximum flow values. To better explain the pneumatic side of the system, a schematic is shown in Fig. 27 representing flow direction.

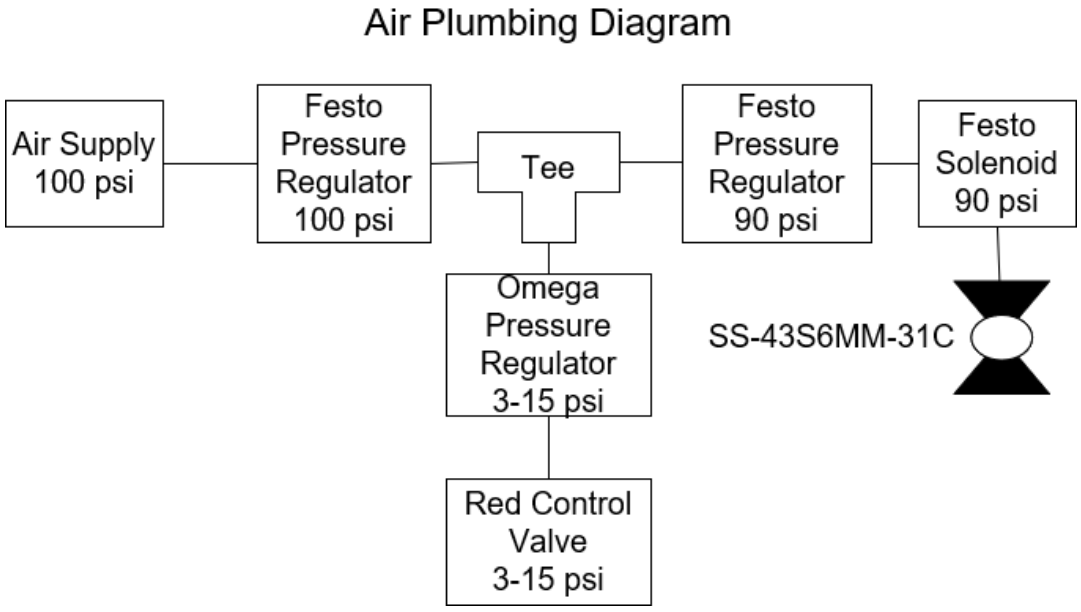

Fig. 27: Air Flow Plumbing Diagram

The air supply fed a Festo pressure regulator adjusted to 100 psi. The flow then split off into a T-connection, with one end having another regulator set to 90 psi and the pressure regulator

attached to the other. The Festo solenoid fed a shut-off valve with 90 psi air. This process meant that whenever the DAQ sent a voltage to the solenoid, the solenoid would permit the air to flow to the manual valve, and the fuel would be allowed to propagate. The pressure regulator received 100 psi airflow and then, based on the current received from the converter, outputted either 3 or 15 psi into the Festo pressure regulator as seen by the red control valve in Fig. 27 below. The red control valve was the mechanical means of actuating the pressure inside the system. Fig. 28 illustrates the red control valve attached to the exhaust of the system. This type of pressure regulation is most commonly referred to as backflow regulation. The amount of exhaust products coming out of the system is regulated by the level of valve opening. The burner is not a closed system, and new gases are constantly being fed into the system; therefore, the idea is to obtain a system that is as close to a steady-state as possible to achieve the desired pressure.

Fig. 28: Control Valve (Left), Solenoid Valve (Right)

3.4.2 PID Loop and Fuel Shutoff

The theory behind the electronically controlled pressure regulation system was the PID loop. Fig. 29 below shows a schematic of the theoretical PID loop. PID stands for the partial, integral, and derivative. The basic theory behind the concept is to drive the feedback to match a set point determined by the user. The three PID terms correspond to three constants, K_P, K_i, and K_d. The proportional tuning termK_P involves correcting the target proportional to the difference value; however, the value is never fully achieved because as the difference approaches zero, so does the correction [50]. Integral tuning $K_i$takes the cumulative error from the P action to increase the correction factor. However, overshoot occurs when the cumulative error is driven to zero. Finally, derivative tuning K_d minimizes the overshoot by slowing the correction factor applied to the target as it gets closer. These three terms were adjusted in LabVIEW to optimize the pressure loop. LabVIEW VI developed for this work is shown in Fig. 30.

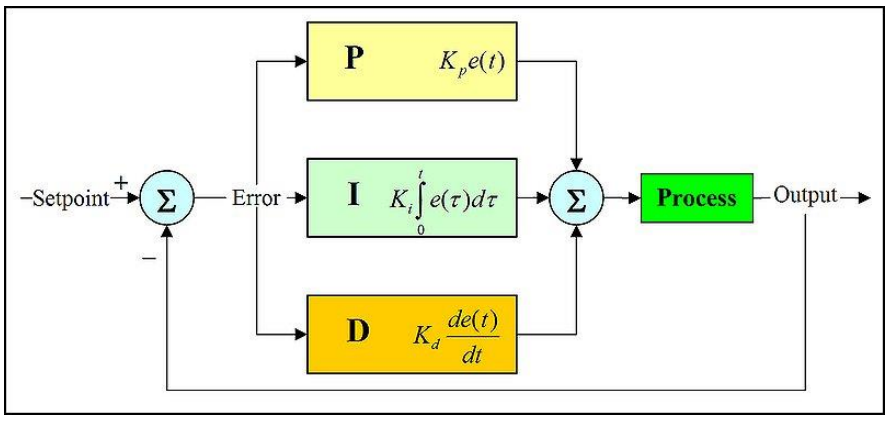

Fig. 29: PID Control Algorithm reprinted from [50]

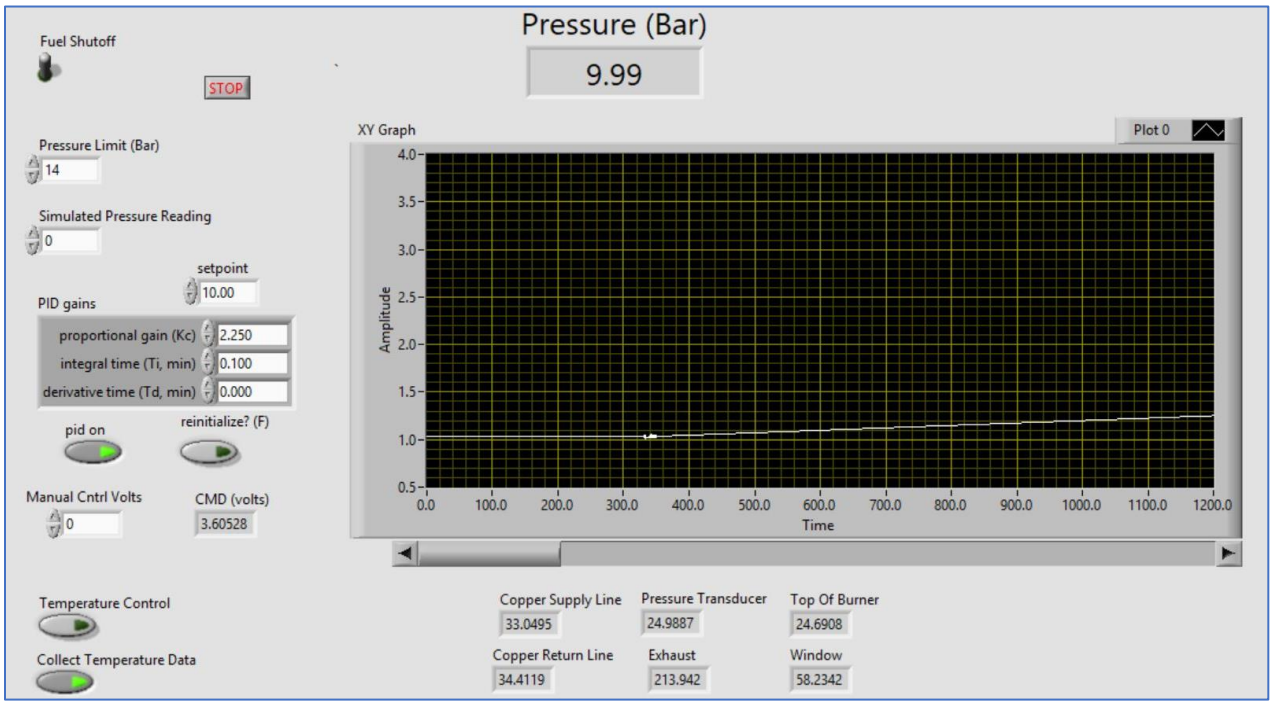

Fig. 30: LabVIEW VI

The PID loop applied to our system as follows: the setpoint pressure was set by the user in the selection button above. The setpoint value then went through the PID loop with values of the constants K_p=2.25, K_i= .1, and K_d=0. The value transformed into a voltage that was then converted into a current via the converter mentioned earlier. The current enters the pressure regulator, which outputted a 3–15 psi signal to the red control valve and then actuated in the upward and downward directions. The details are discussed further in the experimental results section.

3.4.3 Temperature Monitoring

The temperature was monitored and recorded at six key locations that had to be monitored to ensure that the operation of the burner remained safe. These were the water inlet, outlet lines for the 6-mm copper tubing, pressure transducer, the top portion of the burner or "hat," the fused silica windows, and the exhaust. Type-K thermocouples were implemented on the system, and "wire" thermocouples were used for every point except for the exhaust. Depicted in Fig. 31 below is the "probe" type thermocouple used at the exhaust.

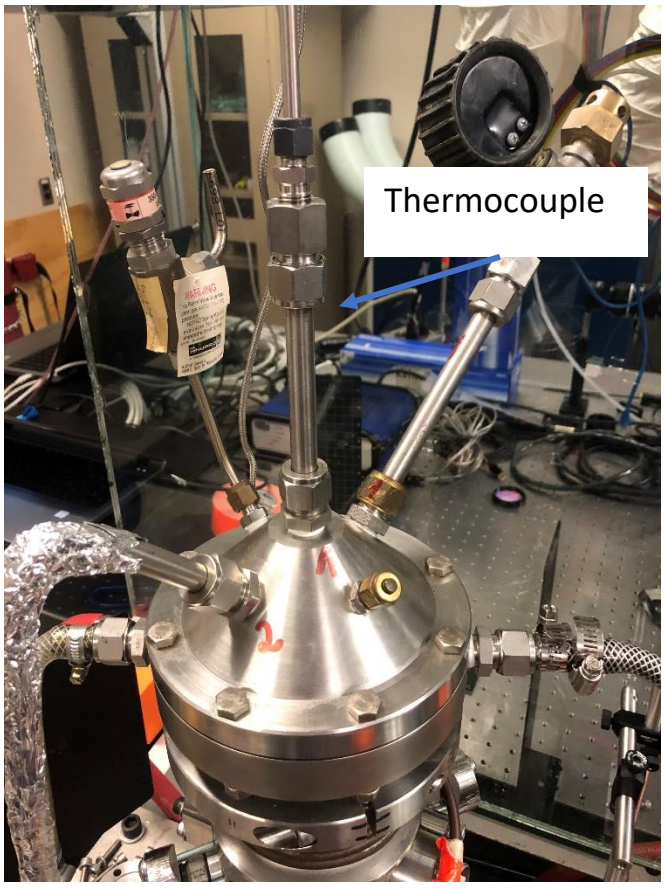

Fig. 31: Exhaust Thermocouple

Out of the temperatures recorded, only one temperature, the exhaust temperature, had a significant increase of over 10 ℃ during the burner operation. The rest of the temperatures did not fluctuate significantly, which attested to the effectiveness of the convective cooling from the guard flow and co-flow. The combined convective effect of the two flows seemed to drive most

of the heat towards the top of the burner. Therefore, the highest temperature recorded in the lower section of the burner where the most thermally sensitive components were located was 40℃ on the windows, which was well within the acceptable thermal limit. The graph in Fig. 32 below shows the change in exhaust temperature with operating pressure for a Φ=1.2 CH_4/air flame.

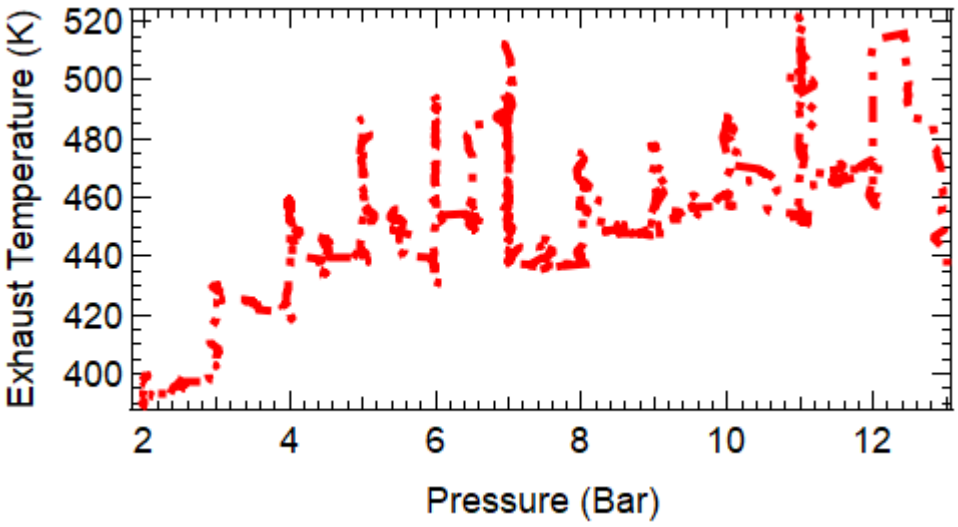

Fig. 32: Exhaust Temperature at Different Operating Pressures

The exhaust temperature showed an interesting behavior. Overall, it is an increasing trendline; however, during the pressure transition periods, the temperature spiked up to approximately 520 K. This behavior is perhaps due to the sudden influx of more combustible gases into the mixture. However, the temperature of 520 K was also well within the thermal limits of the stainless-steel vessel. Overall, the temperature monitoring yielded results that validated the design decisions surrounding the burner, and all tolerances were within the thermal limitations.

3.3.4 Performance Testing

In LabVIEW VI, part of the code was geared towards logging the data after every run. The results of this data validated the code and experimental setup. The results consisted of pressure and temperature measurements. The pressure measurements for a sample test are documented below in Fig. 33, together with a selected section of the graph for the 7-bar section to show the stability of the overall test.

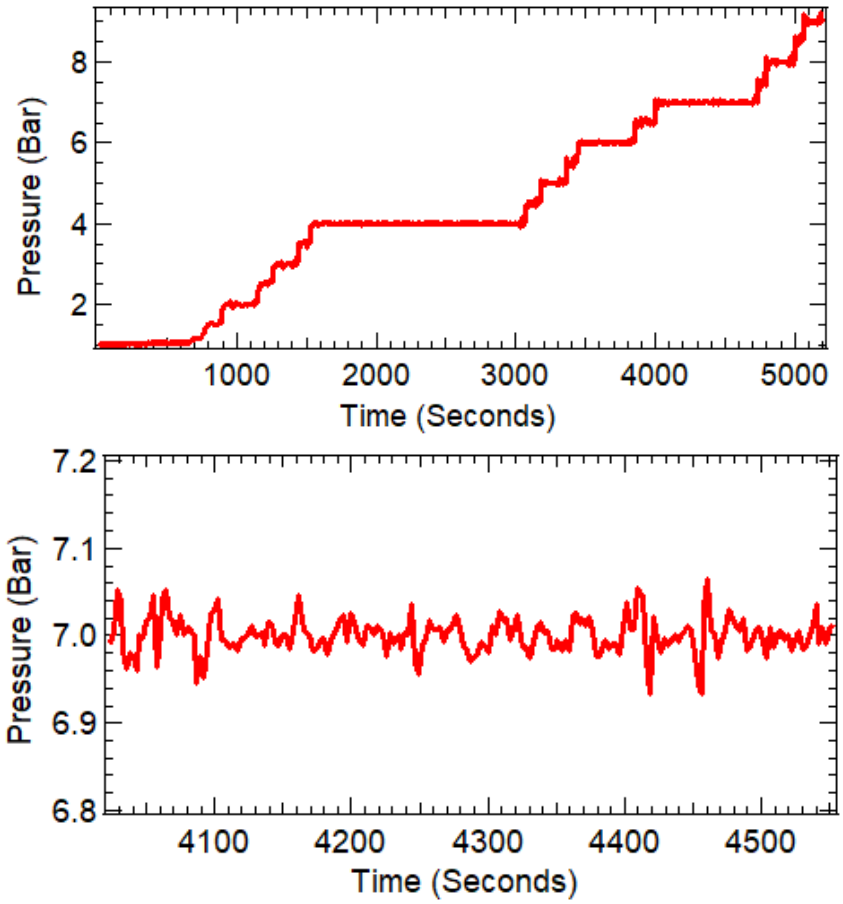

Fig. 33: Operating Pressure Validation Graphs

The top frame of Fig. 33 is a graph of the pressure as a function of time during an experimental run. The flat parts of the graph shown in the bottom flame are where the pressure was kept constant

during data acquisition. The steps in the top frame correspond to the pressure changes throughout the experiment transitioning from one pressure to the other. The graph is relatively stable, but in order to further verify the stability of the pressure system, the data points from the 7-bar region were extracted and plotted for a smaller time range in the bottom frame. A fluctuation of around 0.02 bar was noted for the majority of the measurements, with minor inconsistencies in the system resulting in several large spikes of approximately 0.07 bar. However, transitioning between pressures in the system resulted in the greatest variation in stability throughout the system. This operation resulted in an average variation of 0.3 psi with large spikes, resulting in a variation of 1 psi. We concluded that this variation was within an acceptable experimental uncertainty for the test, and no further corrections are needed to be made during post-processing of the data.

Temperature validation was more involved, as the goal was to validate the cooling system and ensure that the water lines were removing heat effectively. Temperature measurements were recorded during an experimental run. These measurements were then analyzed, and values were calculated for the cooling rate in kJ/s. The graph for the cooling rates is shown in Fig. 34.

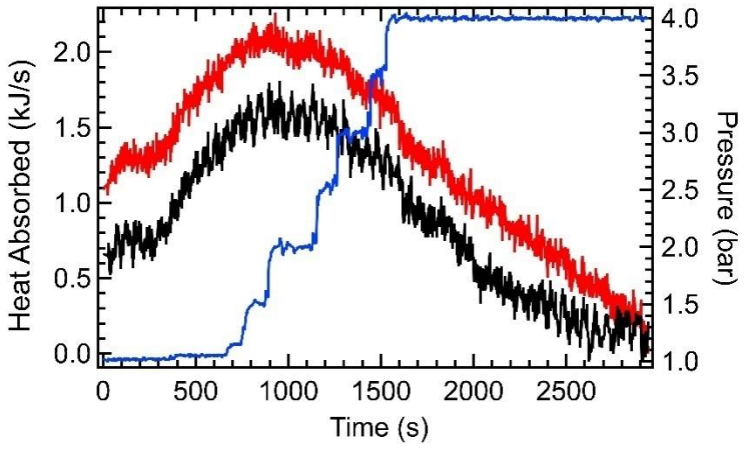

Fig. 34: Temperature Validation Graph

The effectiveness of the cooling rate dropped as the test went on, although this was not altogether surprising based on the fact that the water being used in the system was recycled for each run from the same 50-gallon tank. Essentially, the water started by flowing through the inlets and into the burner cooling channels of the burner. The water then exited the burner through the outlets and back into the 50-gallon tank. This process of continuous recycling over time increased the overall temperature of the water in the tank. The cooling effectiveness was calculated using the difference between the inlet and outlet for the cooling channel and cooling coil. As the test continued, the difference became smaller and smaller because the inlet water temperature constantly increased. This process led to a decrease in efficiency, highlighted in the graph above. It is recommended to add either a chiller to the system or a non-recirculating water system to eliminate this issue in future operations. Overall, the present system was adequate in keeping the burner temperatures sufficiently low for safe operation.

3.5 Safety

The safety of the researchers while operating the high-pressure burner was the highest priority during the experimental tests. Built-in safety features were mentioned in earlier sections, such as burst discs on the airline and electronic shut-off valves. These features undoubtedly contributed to lowering the risk level of operation of the burner, but the most significant measures taken for safety were on the “hat” section of the burner and the blast-proof windows surrounding the facility. The picture in Fig. 35 shows the top portion of the vessel with the backside safety shield in place.

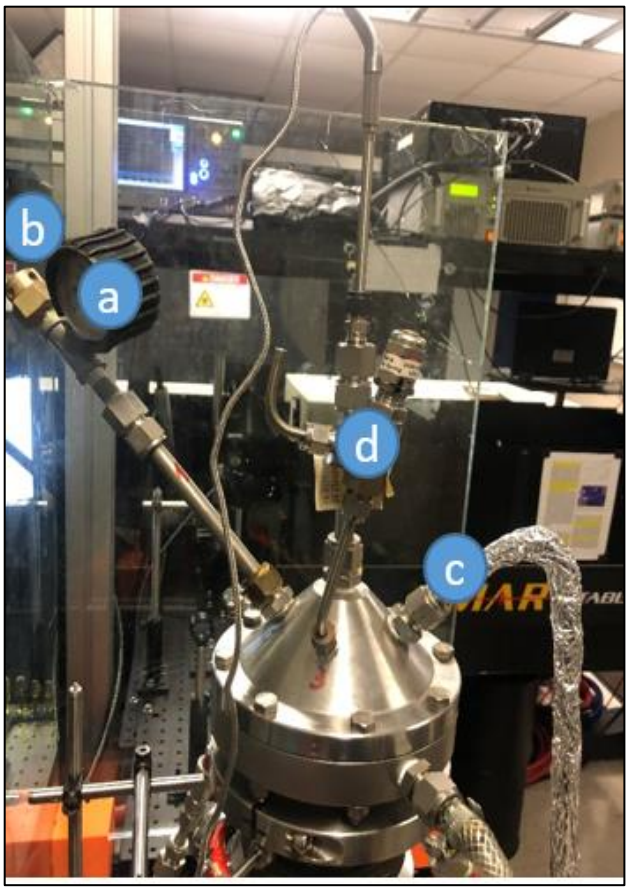

Fig. 35: Safety Mechanisms**;** A) Gauge Pressure Transducer, B) Burst Disc, C) Exhaust, D) Spring Release Valve

Overall, the primary concern centered around the burner is overpressuring and causing mechanical failure in the windows, as this was mechanically the weakest subsystem. The top portion of the burner incorporated a spring valve and another burst disc. The spring valve was set to release at 500 psi, and the burst disc would function at 300 psi. These features created a failsafe in case the burner experienced a significant pressure event. In the case where the burst disc or spring valve did not function properly, and a mechanical failure happened in the burner, blast-proof windows were set up around the exterior of the assembly that mounted the burner on a wheeled frame.

Fig. 36: Blast Windows

The system ensured that equipment and the research scientists would be kept safe in the event that an explosion occurred. Finally, a detailed operating procedure document was prepared and placed together with the burner assembly for all future operators. This document outlined proper operation and shutdown parameters for the burner and is included in the Appendix of this thesis.

4. HIGH-SPEED CHEMILUMINESCENCE IMAGING

4.1 Experimental Apparatus and Procedure

Chemiluminescence images were taken using a Photron FastCam SA-Z camera paired with a LaVision High-Speed Intensified Relay Optics (HS-IRO) module. During chemiluminescence testing, three different emissions were recorded using optical bandpass filters in front of the HS-IRO module. CH* was recorded using a 434 ± 8.5 nm filter, OH* was recorded using a 315 ± 7.5 nm filter, and the broadband chemiluminescence was recorded with no filter. All tests were sampled at a repetition rate of 1 kHz. The HS-IRO gate was set to 0.5 ms, and the intensifier gain was varied for each filter being used but remained constant during the pressure and equivalence ratio scans. Appropriate gain values of 55 for CH*, 45 for OH*, and 40 for broadband emissions were determined during preliminary testing. The spatial resolution of the imaging configuration used was determined to be 19 pixels per mm using a calibration target. The resulting chemiluminescence images were processed by integrating the signal across the flame for each frame. Fig. 37 shows the flame zones used in post-processing. The integration zones were expanded for the unconstrained flame analysis to include the larger flame region and obtain a better understanding of overall oscillations [51].

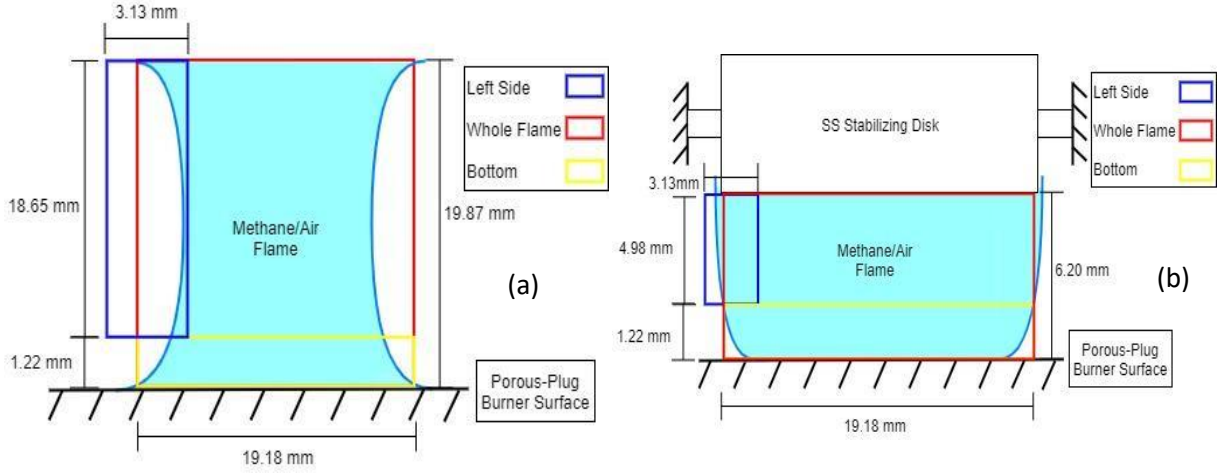

Fig. 37: Chemiluminescence integration zones for (a) unconstrained flame conditions and (b) disk stabilized flame conditions reprinted from [51]

4.2 OH* and CH* Chemiluminescence Results

4.2.1 Flame Structure Studies

Chemiluminescence images were taken for analyzing and characterizing the flame. The first pressure and equivalence ratio scans showed that the flame was not stable in the current burner configuration. The flame oscillated during testing; Fig. 38 shows the oscillations in the broadband, OH*, and CH* chemiluminescence images of the Φ=1.2 flame at 8 bar.

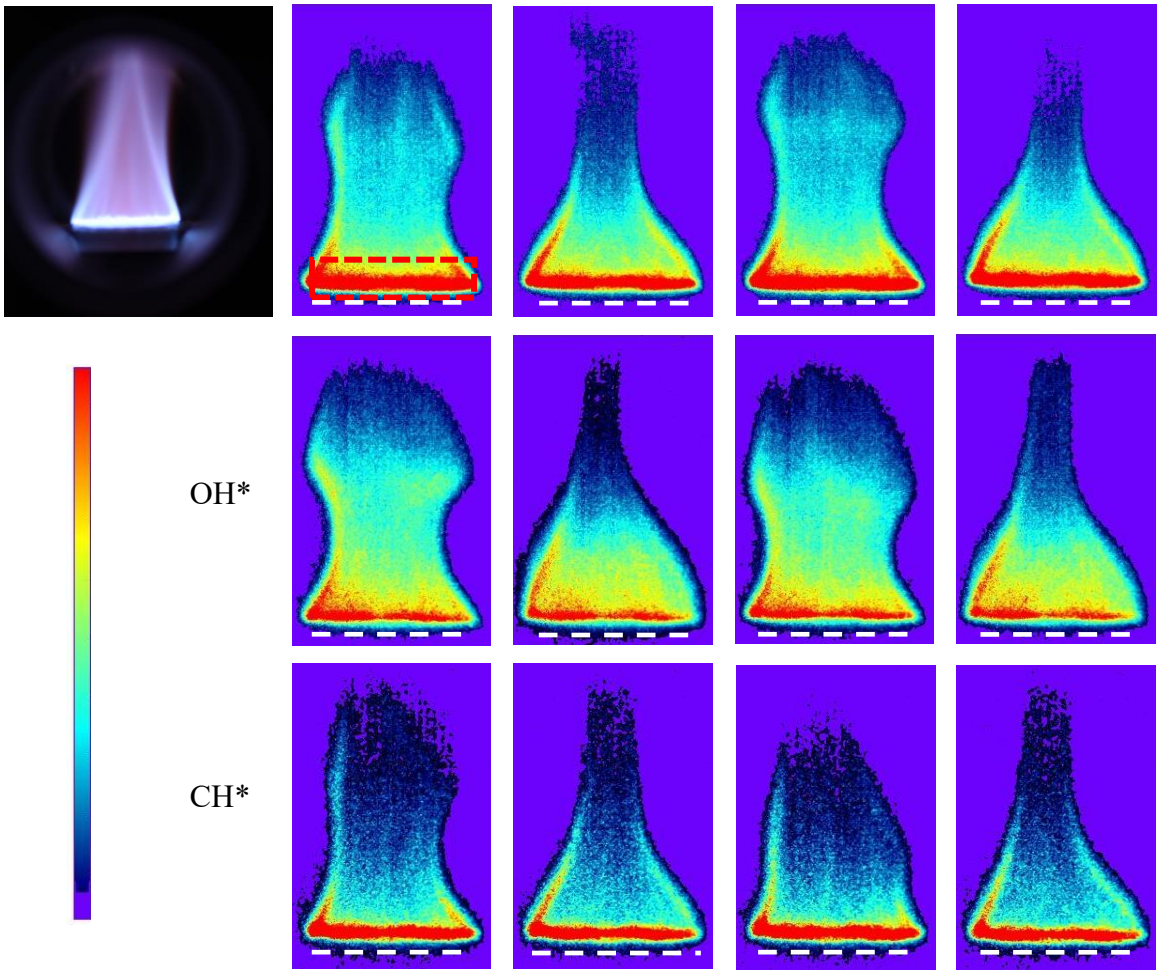

Fig. 38: Experimental flame (top left), broadband chemiluminescence (top row), OH* chemiluminescence (second row), and CH* chemiluminescence (bottom row) at 8 bar Φ=1.2 showing flame oscillations of the unstable flame. Signal integration area (6.20 mm x 19.18 mm) shown in red dashed line.

The first image in each series is the flame at the maximum integrated signal, and the second image is the minimum integrated signal, followed by another maximum and minimum image. Oscillations like these were seen across the entire pressure and equivalence ratio range.

The flame had a similar cone-like structure like that seen in other flat flame burner configurations. However, in other burner configurations at lower pressure, the flame remains in the cone shape and does not deviate much because of the relatively low flow rates involved. The difference for this flame was the high-pressure environment in which the flame was encased. The co-flow offered some resistance to the oscillations present in the flame, but the burner environment was sufficiently turbulent to cause the oscillations seen in the figure above. The OH* and CH* concentration was seen to be at the bottom of the burner closest to the surface where the most immediate combustion occurred, which was modeled previously.

The flame oscillations seen above are undesirable for flame diagnostic techniques; therefore, the unstable flame was stabilized by positioning an axisymmetric stainless-steel disk 8 mm above the burner surface. The disk is held in place by two stainless-steel rods mounted on two auxiliary ports on the pressure vessel, allowing for full optical access to the stable flame. Fig. 39 shows a single shot and averaged OH* and CH* chemiluminescence of the stable flame. These images show the elimination of the flame oscillations, allowing for better flame diagnostics and characterization.

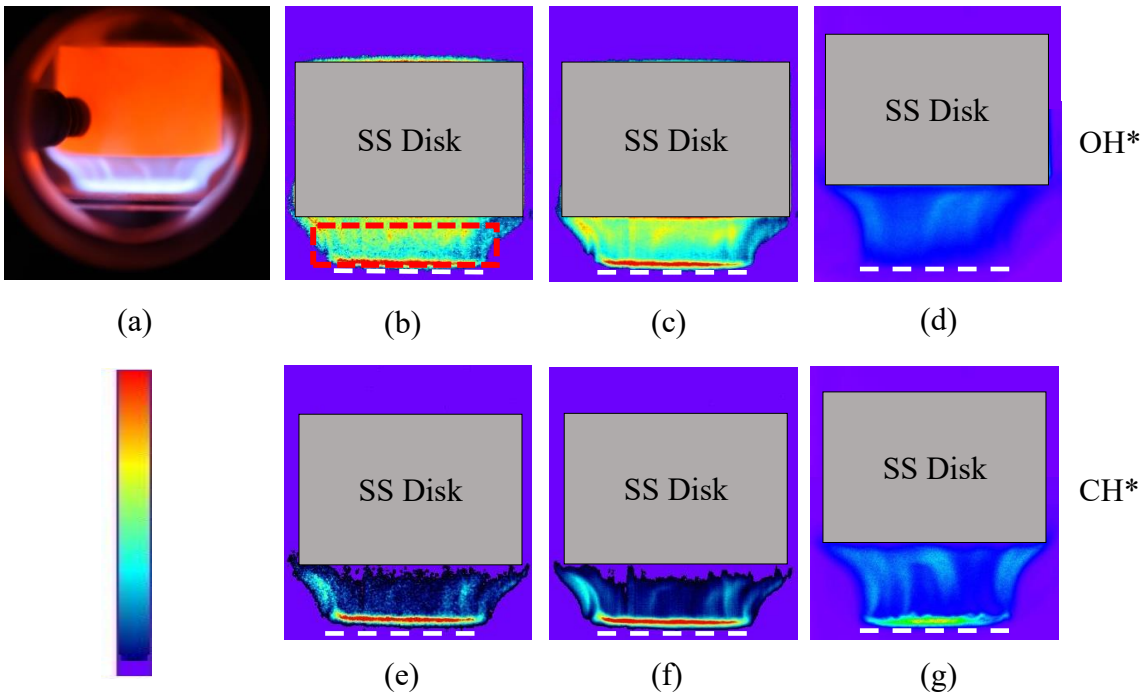

Fig. 39: Experimental flame with a stabilizing stainless-steel disk (a), single shot image (b and e), 1000 shot-averaged image (c and f), and averaged image from an ICCD camera (d and g) at 8 bar Φ=1.2 showing the elimination of flame oscillations with the addition of a stabilizing disk. Signal integration area (6.20 mm x 19.18 mm) shown in red dashed line.

The structure then turned from a cone into more evenly distributed structures that flared upwards at the corners. The stabilizing disk quenched the upper portion of the flame, forcing it to the left and right. The concentration of the radicals once again seemed to be at the bottom of the burner and evenly distributed in the mid-section. An important distinction to make is that the signal is volume-averaged. The camera takes an image that considers all of the chemiluminescence being analyzed all at once. This process does not allow for an accurate representation of each slice of the flame and any discontinuities present as well. The discussion later in this work will highlight the advantages of the OH PLIF technique and how chemiluminescence alone does not allow for a completely accurate representation of the flame structure.

4.2.2 Flame Stability Investigation

Chemiluminescence images were analyzed by integrating the recorded signals in each frame. A 6.20 mm × 19.18 mm integration zone, shown in Fig. 38 and Fig. 39, was used for both the stable and unstable chemiluminescence images. This integration zone was chosen to maximize the area of integration while avoiding saturation from the stabilizing disk. Then, the integrated signal was normalized by the average signal across the integration zone. Fig. 40 shows the normalized OH* chemiluminescence signal of the Φ=1.2 flame at 8 bar plotted as a function of the frame number. The unstable flame OH* chemiluminescence signal experiences large low-frequency oscillations, while the stable flame shows small high-frequency oscillations. The same trend was observed for CH* and broadband chemiluminescence. Using MATLAB's built-in fast Fourier transform (FFT) function, it was found that the dominant frequency of the unstable flame in Fig. 6 was 17 Hz, and the dominant frequency of the stable flame was 178 Hz and 296 Hz. The same fast Fourier transform analysis was conducted for each pressure tested, revealing that as pressure was increased, the frequency of flame oscillations decreased from 19 Hz at 1 bar to 16 Hz at 10 bar. The high-frequency oscillations in the stable flame are likely due to fluctuations in the flame due to the exhaust control valve and PID loop controlling it or the thermo-acoustic fluctuations inside the pressure vessel. Further investigation is needed to determine the cause of the high-frequency noise; however, the stabilizing disk reduced the large flame oscillations to allow for OH-PLIF measurements to be made.

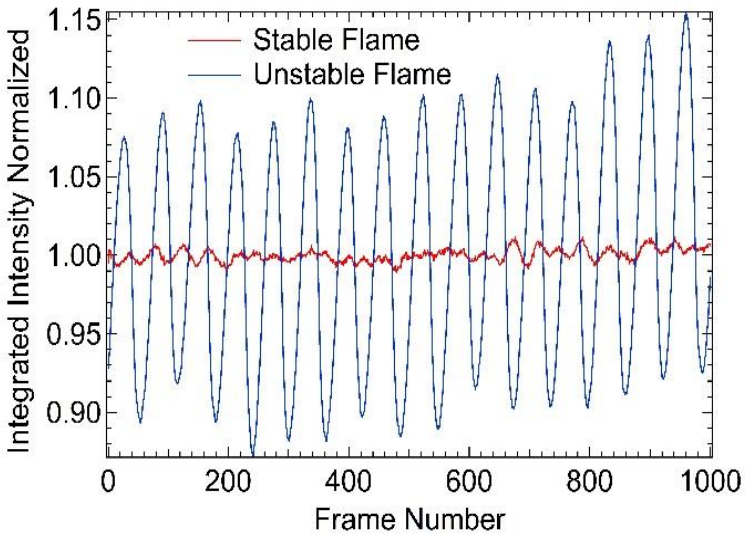

Fig. 40: Total integrated OH* chemiluminescence signal normalized by the average of the stable and unstable Φ=1.2 flame at 8 bar

5. HYDROXYL RADICAL-PLANAR LASER-INDUCED FLUORESCENCE (OH-PLIF) IMAGING

5.1 OH PLIF Experimental

5.1.1 Nanosecond PLIF System

For OH-PLIF imaging studies, a nanosecond-duration Nd:YAG laser (Continuum, Model: Powerlite 8000) outputting the second harmonic at 532 nm was used to pump a tunable dye laser (TDL) (Continuum, Model: ND6000). The output from the dye laser was tuned to 566.61 nm. It was then frequency doubled using a BBO crystal to obtain the desired wavelength of the $Q_1(7)$ line of the OH $A^2\Sigma^+$-$X^2\Pi$ (1,0) band, which corresponds to 283.305 nm in vacuum. The UV beam was then directed using several 45˚ dielectric mirrors to the probe region and converted to a thin laser sheet using a combination of a cylindrical lens (f= -75 mm) and a spherical lens (f=+750 mm). The original UV laser beam diameter was approximately 5 mm. Only the nearly uniform central portion of the UV laser sheet was used to improve the image quality. This configuration produced a laser sheet that propagated through the combustion chamber window into the flame zone and then out into a beam dump through the exit window on the opposite side. An intensified CCD camera (ICCD) (Princeton Instruments, Model: PI-MAX4) fitted with a f=+100-mm-focal-length f/2 UV camera lens (Bernard Halle). The camera was placed perpendicularly to the beam propagation direction to detect the fluorescence signal image from the A←X (1, 1) & (0,0) bands near 308 nm. A bandpass filter (Semrock, Model FF01-315/15) was placed in front of the camera lens to detect the targeted fluorescence wavelength and block out unwanted interferences. The images recorded had resolutions of 1024×1024 pixels. On CCD accumulation of 150 images were used. Thermometry measurements were performed using this same setup but by exciting the $Q_1(5)$ and

$Q_1(14)$ lines and comparing the ratio between the two as discussed by Wang et al. [52]. The OH PLIF experimental apparatus is shown in Fig. 41.

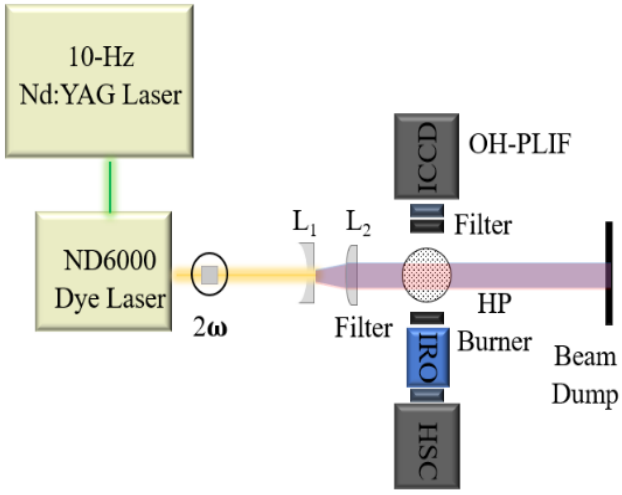

Fig. 41: Experimental Apparatus for High-Pressure OH-PLIF Measurements

.

5.1.2 High-Pressure Burner Experimental Procedure

The components and the basic operating procedure of the high-pressure burner facility were discussed in the previous sections. Atmospheric-pressure flames can be regulated relatively easily and are only adjusted based on the inlet velocity and the equivalence ratio. High-pressure flames, however, require the regulation of the desired pressure and the stability of the flame inside the combustion chamber. For the high-pressure facility at Texas A&M, a standard operating procedure was developed and was successfully implemented up to pressures of 10 bar. First, the LabVIEW VI pressure limit was set to 12 bar for tests at 10 bar, and the PID controller was set to values of gain=2.250, integral time=0.1, and the derivative time to be 0. The pressure setpoint was left at 0.95 bar in order for the controller to start in an open state. The solenoid fuel cutoff was left open, and the PID controller was activated. Gas cylinders fed the burner with methane, air, and nitrogen. The working pressure of cylinders was initially started at 40 psi per the MKS mass flow

controller specifications for 1-bar operation. The initial flow rates for the 1-bar condition were entered into the mass flow controllers, and the flame was ignited with a lighter. Once the flame stability was verified, the optical window holders were secured back onto the vessel, and the pressurization process began. The pressure adjustments were made in increments of 0.5 bar in order to minimize the possibility of an over-pressure event occurring due to the high-pressure jumps.

At any given pressure, the gas cylinders were opened 15 psi more than the previous setpoint pressure. The air and fuel mixture for the premixed portion was adjusted to the next higher setpoint. The corresponding guard and co-flow rates were then elevated to the next pressure setpoint as well. At this point, the pressure inside the chamber should be slightly higher than the setpoint in LabVIEW VI. The pressure was then increased by 0.5 bar in the LABVIEW VI, and the PID loop brings it slowly to that setpoint without extinguishing the flame. After stabilization in the 0.5 bar increment, the co-flow and guard flows were increased again because they naturally decrease due to the pressure fluctuation in the chamber. In subsequent steps, the LabVIEW VI increased the pressure up to the full pressure in steps of 1 bar. The co-flow and guard flow were increased again while ensuring a stable flame. The same procedure was be repeated for all pressures. The detailed operating and shutdown procedures are included in the safety documentation in the Appendix.

5.2 OH PLIF Results & Discussion

5.2.1 Ns OH PLIF Flame Structure

Experimental studies were conducted to investigate the feasibility of the OH-PLIF technique at elevated pressures, which include excitation wavelength scan, laser energy, equivalence ratio, and pressure dependencies. Two-color OH PLIF thermometry measurements were also performed to obtain an accurate representation of the shape and magnitude of the temperature profile within the flame zone.

Laser energy directly affects the OH-PLIF signal. An increase in laser energy will increase the OH-PLIF signal due to the increased output of fluorescence for the targeted molecule due to efficient excitation. To verify that the relationship between laser power and OH-PLIF signal output is linear, as in the case of unsaturated LIF regime, a series of tests were performed at the equivalence ratio of Φ=1.2 while increasing the laser energy in 0.1 mJ steps. The importance of achieving linearity lies in the fact that the energy of the beam is not uniform throughout the projected sheet for the OH-PLIF experimental scheme. The power of the beam increases in the center and decreases steadily radially outwards because of the Gaussian energy distribution of the typical laser beams. Therefore, if it can be confirmed that the LIF signal lies in the linear regime of the laser energy, the PLIF image can be scaled appropriately based on the energy distribution within the laser sheet. Fig. 42 shows that the relationship of PLIF signal vs. laser energy could be characterized as linear for all cases investigated during this study. The only moderate deviation from the linear dependence was observed in the 1-bar case at laser energies above approximately 1 mJ. It should also be noted that during the present experiments, only the middle nearly uniform region of the laser sheet was selected to generate the PLIF image by cutting down the Gaussian wings of the laser sheet by a square slit, thereby eliminating the need for sheet profile corrections.

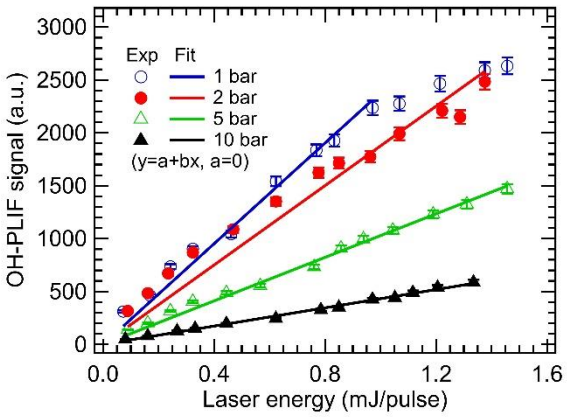

Fig. 42: OH-PLIF Signal as a Function of Laser Energy for Different Pressures

A wavelength scan was also conducted to confirm the location of the $Q_1(7)$ rotational line in the (0,0) band. The LIF signal profile was compared with the theoretical signal generated using the LIFBASE software package [53]. The targeted fluorescence detections of A←X (1, 1) & (0,0) bands presented a weaker fluorescence signal than if utilizing the A–X (1,0) emission near 308 nm resulting from the same band as the excitation wavelength. However, the scattered laser light can be minimized more effectively when (1,1) and (0,0) detection bands are used [35]. The excitation scans at different pressures are shown in Fig. 43 Line broadening can be observed as the pressure is increased. The absorption line shape of the OH radical is most commonly described by the Voigt profile at higher pressures. The line shape is the result of both Doppler and collisional broadening mechanisms. As the pressure increases, the collisional broadening will take over, and the spectrum should become broader, as mentioned before [35]. The excitation spectral line shape is also similar to previous experimental results as the pressure is increased [42,54]. However, no spectral shifting was observed.

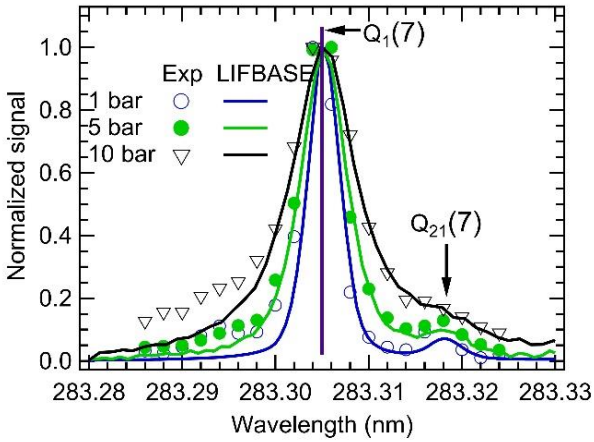

Fig. 43: OH PLIF Wavelength Scan

As mentioned previously, images of the flame were recorded using an ICCD camera equipped with an optical filter to detect the fluorescence signal from the A←X (1, 1) & (0,0) bands. Fig. 44 shows the OH PLIF images from flames at 2-, 5-, and 10-bar pressures for equivalence ratios ranging between 0.7–1.3. The flame is premixed and the leaner equivalence ratios are accurate representations of ideal premixed behavior with a consistent reaction zone across the whole surface of the burner underneath the stabilization disk. However, as the equivalence ratio is increased beyond 1.0 for the 2-bar case and approximately 0.95 for the higher pressures, the middle section of the flame started to diminish, indicating that the reaction zone was shifting towards the outer edges of the burner. The co-flow in our configuration consisted of air that provided the primary reaction zone in the annular region, as evidenced by OH PLIF images. Another item to note is that the signal decreases significantly with the increasing pressure, as shown by the scale factor of each image at 5 and 10-bar cases. To better visualize the flame structure, the signal levels in the 5 and 10-bar cases are multiplied by the shown scaling factor in the plotted image. This behavior of the flame is also captured in the numerical simulations as described in Section 5.2.2.

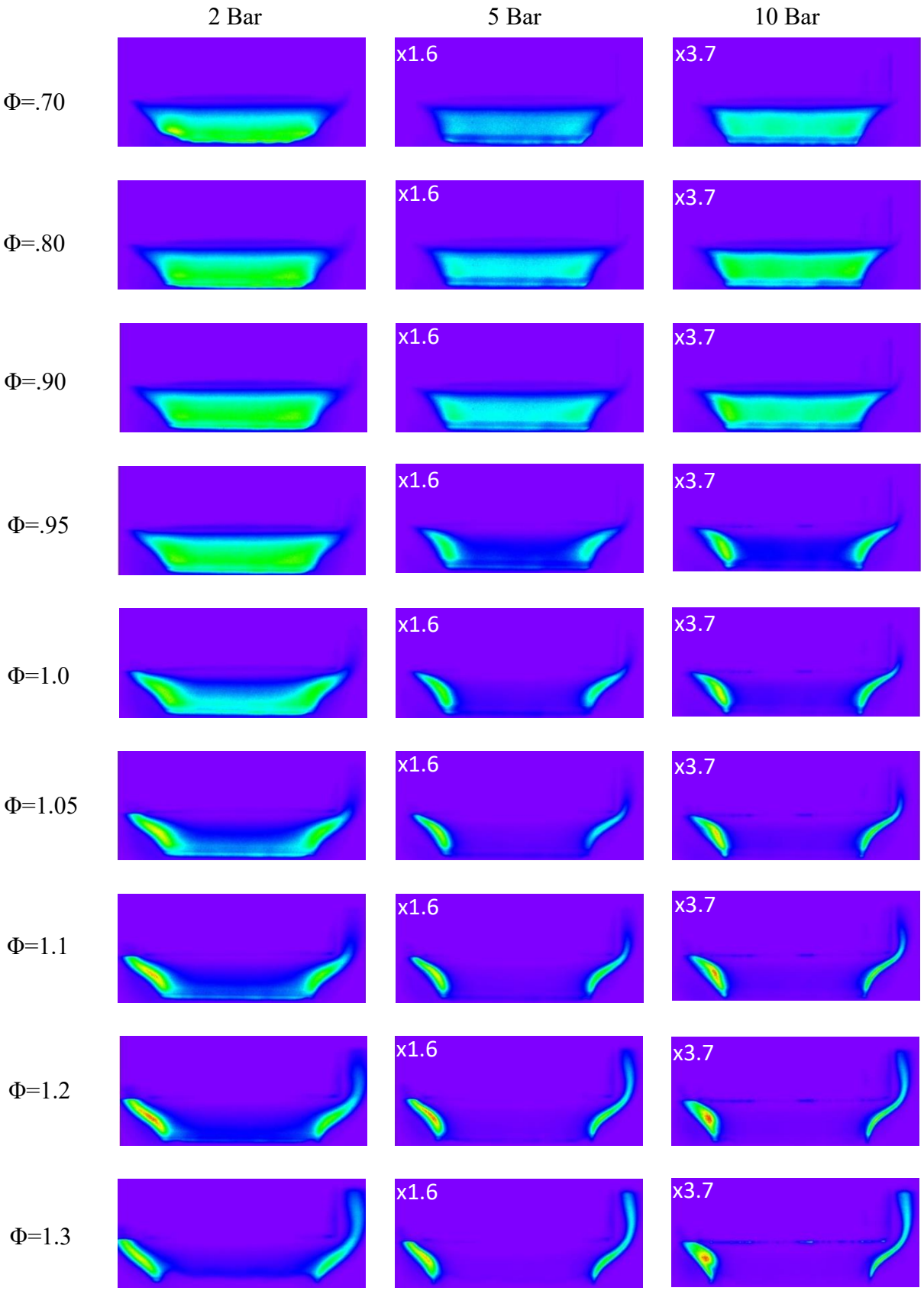

Fig. 44: OH-PLIF as a Function of Equivalence Ratio and Pressure from 2–10 bar.

Radial OH intensity profiles are extracted from the PLIF images and presented below in Fig. 45. These profiles also confirm the conclusions drawn from Fig. 44 above. At the fuel-rich case of Φ=1.2, the OH-PLIF signal in the center decreases to almost zero. This observation is because the premixed flow proceeding into the burner is rich, and therefore the combustion process tends to move towards the outer annular region. The excess fuel makes its way to the edges of the burner surface, where the co-flow of air is mixed with the rich premixed mixture resulting in a diffusion flame front near the edges. This process results in a combustion front on the outside of the burner ring. In the case of Φ = 1.2, two flame fronts present separated by a radial distance of approximately ±10 mm from the centerline. This behavior is usually noted in diffusion-like flames and not in premixed flames. More investigations are planned to further explore this observation in future studies. The presence of the stabilization disk undoubtedly played a significant role in changing the flame structure at higher equivalence ratios. The stagnation plane results in trapping the combustion in the pockets, as observed. In the case for Φ = 1.2 and 2 bar, for example, the flame is noticeably asymmetric. While the fuel-rich cases for 5 and 10 bar are also asymmetric, this behavior can be attributed to non-uniform flow from the sintered metal surface of the burner and flow pattern created by slight off-centering of the stainless steel disk. The laser sheet is propagating from right to left; hence the region behind the disk is not illuminated, resulting in the dark region above the bottom surface of the disk on the left side of all images, in particular, at the fuel-rich flame conditions.

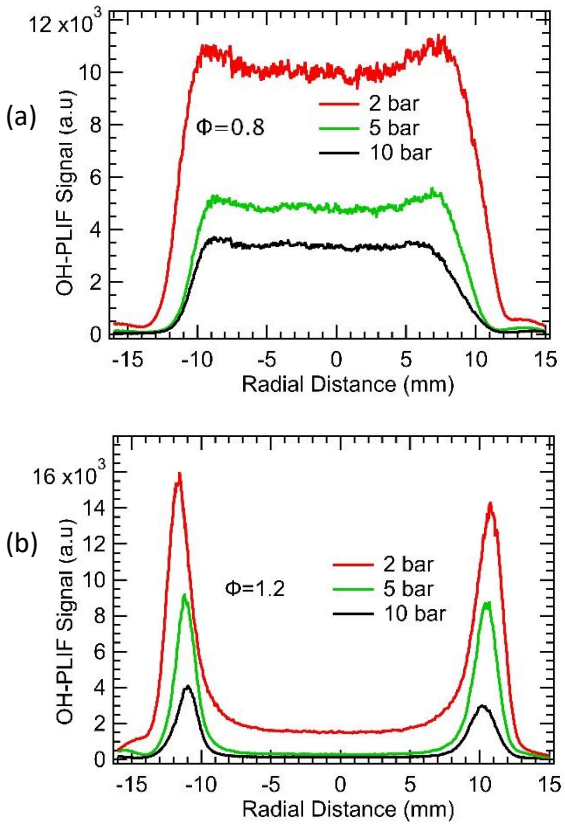

Fig. 45: Radial OH Signal Profiles Obtained Following the $Q_1(5)$ Excitation Wavelength for (a) Φ =0.8 (b) Φ =1.2 Cases.

Quenching corrections for OH profiles at different pressures were applied and compared to the experimental pressure scans as shown below in Fig. 46. Although quenching corrected OH profiles are slightly higher as compared to uncorrected profiles, they do not account for the significant signal drop as the pressure is increased from 1–10 bar. However, the OH number density should increase proportionately with the pressure. Other interferences such as line broadening, laser absorption, and fluorescence signal trapping are to be considered to account for large signal drops at elevated pressures.

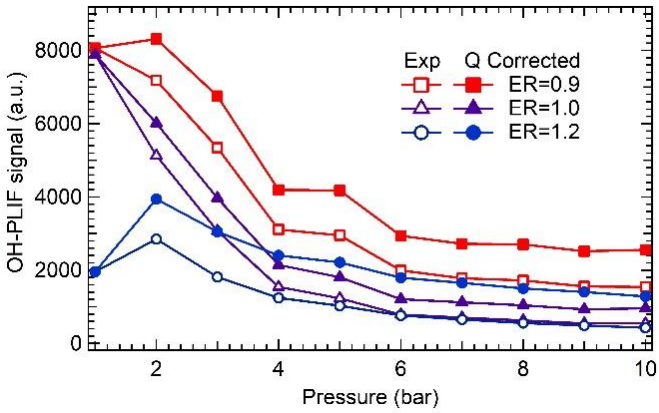

Fig. 46: Quenching Corrected OH PLIF Signal as a Function of Pressure.

One point of interest is the correlation of the strength of the OH-PLIF signal to the equivalence ratio. Combustion efficiency is maximized at Φ =1.0, and therefore the highest OH-PLIF signal should occur at that flame condition as well. Fig. 47 shows the number density of the hydroxyl radical at three different pressures while varying the equivalence ratio from lean to rich. CANTERA flame simulations were conducted and are plotted against the experimental data [55]. The experimental and model results are similar as seen in the trend lines, yet the peak location was initially shifted to the lean side in the experimental cases compared to the model. After the experiment was completed, a calibration was performed for the MKS mass-flow controllers to obtain accurate values of the actual flowrates. The calibration results suggested the equivalence ratio should be shifted by approximately 0.05 to the richer side for each case to account for the offset in the mass flow controllers. That offset is applied in the plots shown in Fig. 47. For the 5 and 10 bar cases, the offset is still not sufficient to match experimental and model results completely. The increasing pressure in the system may have contributed to a certain degree to the increased uncertainty and shift in equivalence ratio.

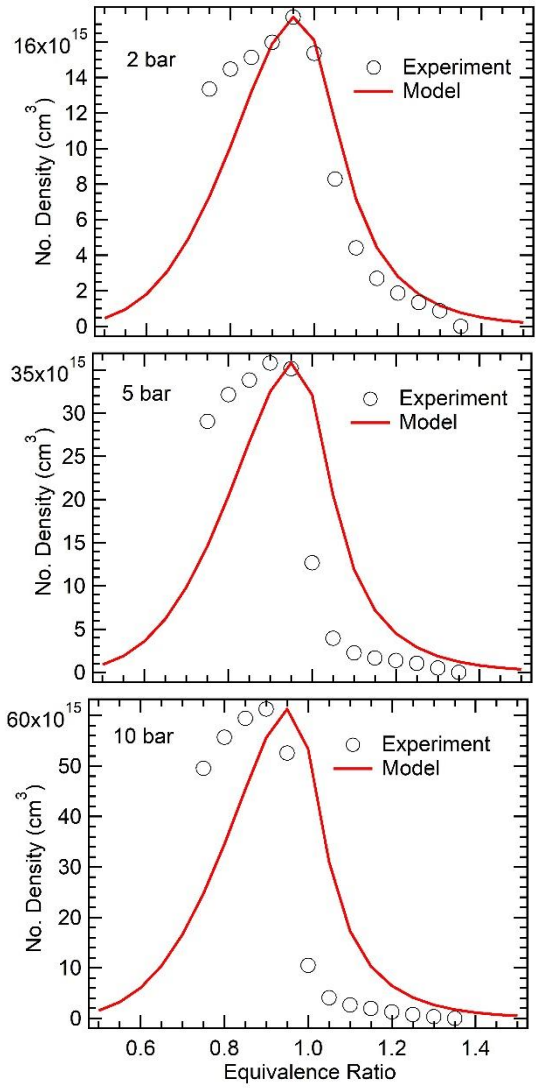

Fig. 47: OH-PLIF Equivalence Ratio Scan at Three Pressures (a) 2 bar (b) 5 bar (c) 10 bar, Shown Together with the OH Number Densities Calculated Using CANTERA Code.

Experimental data was then recorded by tuning the excitation laser to $Q_1(5)$ and $Q_1(14)$ rotational lines for use in thermometry measurements. Several investigations have found that the pair of $Q_1(5)$ and $Q_1(14)$ rotational lines of the OH $A^2\Sigma+\rightarrow X^2\prod$ (1,0) electronic transitions are the most accurate line pairs for OH-PLIF thermometry [56]. Two-line thermometry results are discussed in the next section, together with initial work of numerical simulations of the present flame conditions for qualitative comparison.

5.2.2 Ns OH PLIF Thermometry

The next phase of the experiment involved performing thermometry measurements to further characterize the flame. Other researchers have already investigated higher pressure flames, in particular, at leaner equivalence ratios [31]. As mentioned before for the two-color thermometry procedure, the two rotational transitions, $Q_1(5)$ at 283.750 nm and $Q_1(14)$ at 286.456 nm of the OH $A^2\Sigma+-X^2\prod$ (1,0) band were used, followed by detecting the fluorescence emission in the OH (0,0) and (1,1) bands. The ratio of average OH-PLIF signals from the transition lines was used to determine the flame temperature based on previous experimental work by Wang et. al. [52]. Fig. 48 shows a direct comparison for the temperature distribution of the flame at 2 and 10 bar. The temperatures of the 10-bar flame are significantly higher than the 2 bar flame, but the 2 bar flame had a more homogenous structure. At the richer flame equivalence ratios, for the 10-bar case, the signal disappeared in the middle, which was consistent with the OH PLIF results discussed above. This observation also provides further evidence of the absence of the flame zone and decrease in combustion in the central part at these equivalence ratios, as temperature increases are commonly associated with evidence of higher combustion efficiency.

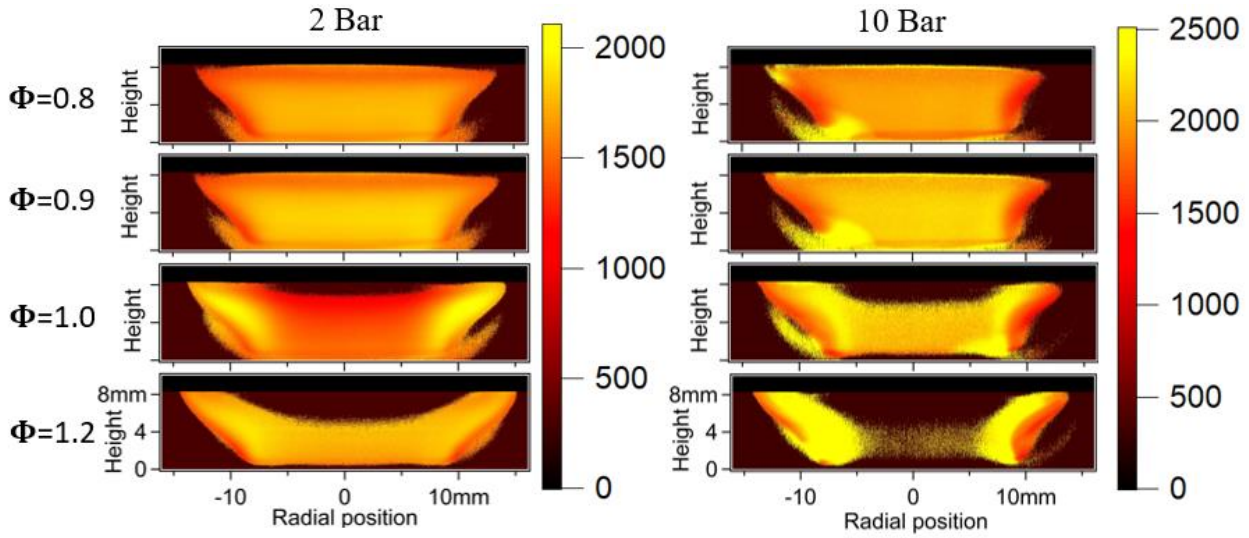

Fig. 48: 2D Temperature Profiles Obtained Using the Two-Color OH-PLIF Method for (a) 2-bar, and (b) 10-bar flame for Varying Equivalence Ratio

Fig. 48 shows the radial temperature distribution of the flame at different equivalence ratios and heights above the burner. As also demonstrated before, radial temperatures depend heavily on equivalence ratio and pressure. Fig. 49 (a) and (c) indicate the temperature increases at higher pressures, which is consistent with some cases studying the NO concentration in high-pressure flames [57]. The stabilizing disk most likely had a significant effect on the temperature. The disk tends to trap heat and radiate back to the burner surface. One item to note is the fact that the temperature appeared constant throughout the center for all pressures. This observation, however, is not altogether surprising as the images presented previously seem to indicate a uniform temperature distribution at the leaner equivalence ratios. The temperature as a function of height above the burner seemed consistent with the pressure variation at a fixed equivalence ratio, which also agreed with the images produced previously.

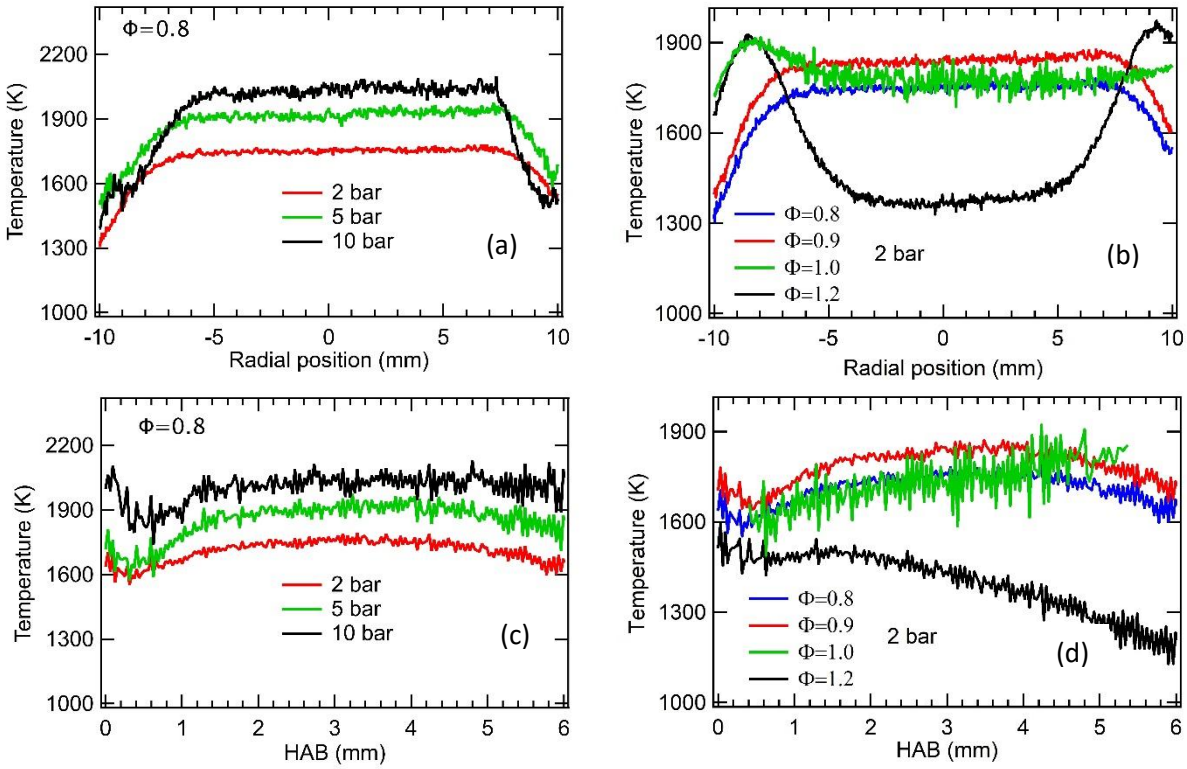

Fig. 49: Radial Temperature Profiles at (a) Φ =0.8 for Varying Pressure, (b) 2 bar for Varying Equivalence Ratio, as a Function of Height-Above-the-Burner for (c) Different Pressures and (d) Different Equivalence Ratios

The experimental results recorded for the OH profiles and thermometry data were also simulated in a model for comparison. This model simulates a high-pressure burner configuration using the ANSYS Fluent software package by incorporating a partially premixed combustion model. Fig. 50 shows the model of the computational domain used for the simulations. The left side is the inlet where a premixed mixture of CH_4-air flows through a section, and a co-flow of air surrounds the combustible mixture. A 2D axisymmetric solver was selected, allowing the simulations to be conducted only at half of the domain. The axisymmetric solver requires the surface to be created on the positive Y of the X-axis and the axis to lie on the X-axis.

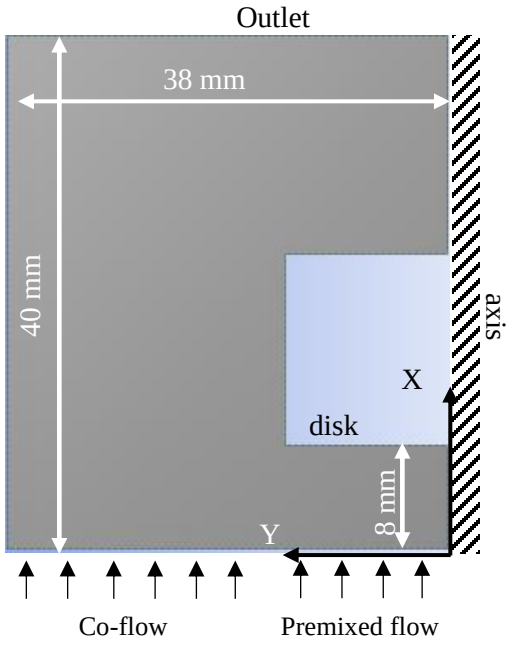

Fig. 50: Computational Domain for 2D Flame Calculations

The domain extends to 40 mm in the X-direction and 38 mm in the Y-direction. Because of the small domain size, we were able to discretize the model into uniformly fine grids at every location. The grids were generated with a face meshing tool, each element being quadrilateral in shape and 100 μm in size. For the larger domain, a bias factor could be applied to minimize the grid size in the region of interest. The mesh statistics created are highlighted in Table 1.

Table 1: Mesh statistics

Statistics	**Values**
Nodes	119021
Elements	118150
Minimum orthogonal quality	0.999
Maximum orthogonal skewness	5.952E-07
Maximum aspect ratio	1.417

Once the mesh is generated, the boundary conditions are provided in the setup section. The inlet flow conditions obtained from the experiments were provided as mass flow rate and set normal to the boundary. The outlet was defined as a pressure outlet. A wall boundary condition of estimated equilibrium temperature 1000 K is provided to the disk surface facing the inlet. In Solution methods, a SIMPLE scheme algorithm was used. It is often preferred for steady-state problems owing to its ability to converge solutions quickly. A second-order upwind setting was set for all solvers (momentum, turbulent kinetic energy, energy, and progress variable) to increase the accuracy of the solution. In addition, a convergence criterion for each residual was set to 1E-04 except for the energy for which it was set to 1E-06. The domain was initialized as a Hybrid initialization. A small rectangular region was adapted near air-fuel, allowing the entire region to be recalculated with combustion included. The number of iterations was set to 1E+04, and the simulation was left for convergence.

Fig. 51 shows a qualitative comparison of OH distribution profiles obtained from the experiment and the above model. The model predictions show that OH distribution is centered in lean cases, while the signals become annular as the flame becomes richer. Further, the signals are reduced on both rich and lean cases as compared to stoichiometric ones. Comparison of OH distribution profiles for CH_4-air flame at P = 2 bar is shown in the top two rows and P = 10 bar on the bottom two rows. The cases of $\Phi = 0.8$ are shown in the left column, $\Phi = 1.0$ in the middle column, and $\Phi = 1.2$ in the right column. The first and third rows represent OH signals obtained from the experiment and the second and fourth rows are respective calculations. The qualitative agreement between the experiment and numerical predictions further strengthens the creditability of the experimental results presented before.

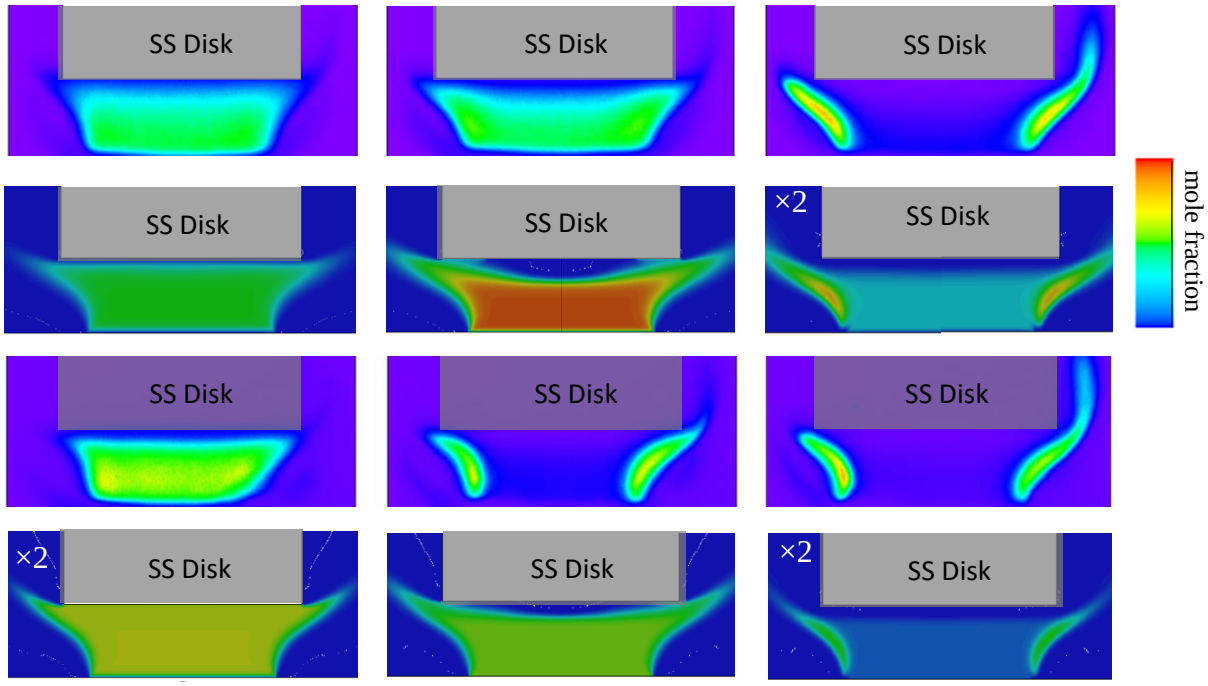

Fig. 51: Comparison of Experimental and Calculated OH Distribution Profiles

6. CONCLUSIONS & RECOMMENDATIONS FOR FUTURE WORK

6.1 Conclusions

This thesis reports the development and characterization of a high-pressure burner facility using high-speed chemiluminescence, OH-PLIF, and thermometry. Several engineering sub-systems were successfully designed and implemented for an existing high-pressure vessel and burner. The systems proved to be reliable and able to successfully operate the burner safely at pressures up to 10 bar. Advanced laser diagnostics were used to investigate the combustion behavior of the burner and provide an accurate representation of flame structures and temperature. The hydroxyl radical distribution was studied using the $Q_1(7)$ rotational transition of the OH $A^2\Sigma^+$-$X^2\Pi$ (1,0) electronic band. Thermometry measurements were performed using the $Q_1(5)$ and $Q_1(14)$ rotational line pair and compared with numerical flame calculations.

For chemiluminescence images, OH* and CH* emissions were recorded at 1-kHz speed using optical bandpass filters in front of the high-speed camera system. The chemiluminescence measurements highlighted the oscillations of the flame during burner operation. The subsequent partial elimination of these oscillations was achieved by the addition of the stabilization disk. The OH PLIF experiments demonstrated several key results that are consistent with the previous literature. Pressure broadening of the OH excitation line was documented, and it followed the model generated in the LIFBASE remarkably well. The transition from premixed to the diffusion-like flame structure at a high flame equivalence ratio is also documented. During the initial imaging phase, this behavior was evident as the signal at richer equivalence ratios and higher pressures reduced to almost zero in the middle region and started to operate more like a diffusion flame. This behavior, in comparison to the optimum height of the disk above the burner surface, needs further investigation.

A detailed quenching correction was implemented in order to account for the signal loss from collisional quenching dominating at elevated pressures. The quenching mechanism and other signal loss pathways such as fluorescence trapping and laser beam absorption need further investigations to describe the decrease in the intensity of the signal as pressure increased. At 10-bar pressure, the OH signal peaks close to an equivalence ratio of $\Phi = 0.95$. Furthermore, the overall OH signal decreased as a function of pressure. However, the increase in the number density of the OH radical associated with increasing pressure should have produced more OH in the flame zone. The signals had to be scaled by a factor of ×4 at 10 bar in order to compare the signals from lower pressures. Thermometry measurements revealed that the temperature distribution moved away from the centerline at richer equivalence ratios, which was consistent with the predicted findings from the OH-PLIF signal and numerical simulations. The temperature profiles remained uniform and symmetric for rich and lean flames for almost all pressure conditions.

6.2 Recommendations for Future Work

Future work will include extending the operating pressure range of the vessel to 50 bar and applying numerous other laser diagnostics to increase the fundamental understanding of the high-pressure combustion process ate gas-turbine relevant conditions. Reaching a pressure of 50 bar will be a significant technical challenge. The main issues involved with achieving this pressure are incorporating different mass flow controllers, adding higher factors of safety for structural components, and increasing cooling capabilities for stable burner operation. Recommended mass flow controllers for these higher pressures have been identified, together with flow adjusting capabilities that are electronically controlled. Structural components such as the optical windows and safety valves will have to be replaced or redesigned for the conditions imposed on the burner at 50 bar. Cooling capabilities in the 10-bar setup proved to decrease over time; therefore, it is

recommended to obtain a chiller unit capable of providing continuous cooling for the entire system. Lastly, additional optical and laser-based diagnostics are recommended to better characterize these flames and to obtain a comprehensive physio-chemical data set for advanced combustion studies.

REFERENCES

1. Mom, A. J. A. (2013). 1 - Introduction to gas turbines. Modern Gas Turbine Systems. P. Jansohn, Woodhead Publishing**:** 3-20.

2. Leschowski, M., T. Dreier and C. Schulz (2014). "An automated thermophoretic soot sampling device for laboratory-scale high-pressure flames." Review of Scientific Instruments **85**: 045103-045103.

3. Frank, J., M. Miller and M. Allen (1999). Imaging of laser-induced fluorescence in a high-pressure combustor. 37th Aerospace Sciences Meeting and Exhibit, American Institute of Aeronautics and Astronautics.

4. Atakan, B., J. Heinze and U. E. Meier (1997). "OH laser-induced fluorescence at high pressures: spectroscopic and two-dimensional measurements exciting the A–X (1,0) transition." Applied Physics B **64**(5): 585-591.

5. Kim, T. Y., Y. H. Kim, Y. J. Ahn, S. Choi and O. C. Kwon (2019). "Combustion stability of inverse oxygen/hydrogen coaxial jet flames at high pressure." Energy **180**: 121-132.

6. Lawitzki, A., I. Plath, W. Stricker, J. Bittner, U. Meier, et al. (1990). "Laser-induced fluorescence determination of flame temperatures in comparison with CARS measurements." Applied Physics B **50**(6): 513-518.

7. Matynia, A., M. Idir, J. Molet, C. Roche, S. de Persis, et al. (2012). "Absolute OH concentration profiles measurements in high pressure counterflow flames by coupling LIF, PLIF, and absorption techniques." Applied Physics B **108**(2): 393-405.

8. Bessler, W. G., C. Schulz, T. Lee, J. B. Jeffries and R. K. Hanson (2002). "Strategies for laser-induced fluorescence detection of nitric oxide in high-pressure flames. I. A–Xexcitation." Applied Optics **41**(18): 3547-3557.

9. Hofmann, M., W. G. Bessler, C. Schulz and H. Jander (2003). "Laser-induced incandescence for soot diagnostics at high pressures." Applied Optics **42**(12): 2052-2062.

10. Boxx, I., C. Slabaugh, P. Kutne, R. P. Lucht and W. Meier (2015). "3kHz PIV/OH-PLIF measurements in a gas turbine combustor at elevated pressure." Proceedings of the Combustion Institute **35**(3): 3793-3802.

11. Lee, T. H., Stanford University., & Hanson, Ronald K. (2006). “Strategies for nitric oxide laser-induced-fluorescence in high-pressure combustion systems.”

12. Wu, Y. (2016). Experimental investigation of laminar flame speeds of kerosene fuel and second generation biofuels in elevated conditions of pressure and preheat temperature.

13. Hofmann, M., W. G. Bessler, C. Schulz and H. Jander (2003). "Laser-induced incandescence for soot diagnostics at high pressures." Applied Optics **42**(12): 2052-2062.

14. High-Speed OH* and CH* Chemiluminescence Imaging Diagnostics in Spherically Expanding Flames**,** Pradeep Parajuli[1], Tyler T. Paschal[1], Mattias A. Turner[2], Yejun Wang[3], Eric L. Petersen[4], and Waruna D. Kulatilaka[5] AIAA Journal, In Review (2020).

15. Nori, V. N. and J. M. Seitzman (2009). "CH∗ chemiluminescence modeling for combustion diagnostics." Proceedings of the Combustion Institute **32**(1): 895-903.

16. Arndt, C. M., M. Severin, C. Dem, M. Stöhr, A. M. Steinberg, et al. (2015). "Experimental analysis of thermo-acoustic instabilities in a generic gas turbine combustor by phase-correlated PIV, chemiluminescence, and laser Raman scattering measurements." Experiments in Fluids **56**(4): 69.

17. Sick, V. (2013). "High speed imaging in fundamental and applied combustion research." Proceedings of the Combustion Institute **34**(2): 3509-3530.

18. Boxx, I., C. Heeger, R. Gordon, B. Böhm, M. Aigner, et al. (2009). "Simultaneous three-component PIV/OH-PLIF measurements of a turbulent lifted, C3H8-Argon jet diffusion flame at 1.5 kHz repetition rate." Proceedings of the Combustion Institute **32**: 905-912.

19. . Böhm, B., C. Heeger, R. Gordon and A. Dreizler (2011). "New Perspectives on Turbulent Combustion: MultiParameter High-Speed Planar Laser Diagnostics." Flow Turbulence and Combustion - FLOW TURBUL COMBUST **86**: 313-341.

20. Muruganandam, T., S. Nair, D. Scarborough, Y. Neumeier, J. Jagoda, et al. (2005). "Active Control of Lean Blowout for Turbine Engine Combustors." Journal of Propulsion and Power - J PROPUL POWER **21**: 807-814.

21. Smith, J. and V. Sick (2007). "The Prospects of Using Alcohol-Based Fuels in Stratified-Charge Spark-Ignition Engines." SAE Technical Papers.

22. Ko, Y., R. W. Anderson and V. S. Arpaci (1991). "Spark ignition of propane-air mixtures near the minimum ignition energy: Part I. An experimental study." Combustion and Flame **83**(1): 75-87.

23. J.D. Smith, V. Sick, Combustion in Spark Ignition Engines, in: J. Jarosinski, Bernard Veyssiere (Eds.), Combustion Phenomena: Selected Mechanisms of Flame Formation Propagation and Extinction, CRC Press, Taylor & Francis Group, Baton Raton, FL, 2009, p. 220.

24. Z. Filipi, V. Sick, Combustion in Diesel Engines, in: J. Jarosinski, B. Veyssiere (Eds.), Combustion Phenomena: Selected Mechanisms of Flame Formation, Propagation, and Extinction, CRC Press, Taylor and Francis Group, Baton Raton, FL, 2009, p. 220.

25. Han, K.-M., A. Velji and U. Spicher (2007). "3D optical fiber technique for spatial flame analysis in internal combustion engines." MTZ worldwide **68**(4): 24-27.

26. Stojkovic, B. D., T. D. Fansler, M. C. Drake and V. Sick (2005). "High-speed imaging of OH* and soot temperature and concentration in a stratified-charge direct-injection gasoline engine." Proceedings of the Combustion Institute **30**(2): 2657-2665.

27. Zare, R. N. (2012). "My Life with LIF: A Personal Account of Developing Laser-Induced Fluorescence." Annual Review of Analytical Chemistry **5**(1): 1-14.

28. "What Is Laser Induced Fluorescence?: LIF Experiment." *Edinburgh Instruments*, Edinburgh Instruments, 18 Feb. 2021, www.edinst.com/blog/what-is-laser-induced-fluorescence/.

29. Grisch, F. and M. Orain (2009). "Role of Planar Laser-Induced Fluorescence in Combustion Research." AerospaceLab(1): p. 1-14.

30. Houwing, A. F. P., D. R. Smith, J. S. Fox, P. Danehy and N. Mudford (2001). "Laminar boundary layer separation at a fin-body junction in a hypersonic flow." Shock Waves **11**: 31-42.

31. Bessler, W. G., F. Hildenbrand and C. Schulz (2001). "Two-Line Laser-Induced Fluorescence Imaging of Vibrational Temperatures in a NO-Seeded Flame." Appl Opt **40**(6): 748-756.

32. Rothe, E. W. and P. Andresen (1997). "Application of tunable excimer lasers to combustion diagnostics: a review." Applied Optics **36**(18): 3971-4033.

33. Houwing, A. F. P., D. R. Smith, J. S. Fox, P. M. Danehy and N. R. Mudford (2001). "Laminar boundary layer separation at a fin-body junction in a hypersonic flow." Shock Waves **11**(1): 31-42.

34. Frank, J., M. Miller and M. Allen (1999). Imaging of laser-induced fluorescence in a high-pressure combustor. 37th Aerospace Sciences Meeting and Exhibit, American Institute of Aeronautics and Astronautics.

35. Singla, G., P. Scouflaire, C. Rolon and S. Candel (2006). "Planar laser-induced fluorescence of OH in high-pressure cryogenic LOx/GH2 jet flames." Combustion and Flame **144**(1): 151-169.

36. Allen, M. and R. Hanson (1986). "Planar Laser-Induced-Fluorescence Monitoring Of OH In A Spray Flame." Optical Engineering **25**(12): 251309.

37. Tanahashi, M., S. Murakami, G.-M. Choi, Y. Fukuchi and T. Miyauchi (2005). "Simultaneous CH–OH PLIF and stereoscopic PIV measurements of turbulent premixed flames." Proceedings of the Combustion Institute **30**(1): 1665-1672.

38. Sadanandan, R., M. Stöhr and W. Meier (2008). "Simultaneous OH-PLIF and PIV measurements in a gas turbine model combustor." Applied Physics B **90**(3): 609-618.

39. Donbar, J. M., J. F. Driscoll and C. D. Carter (2000). "Reaction zone structure in turbulent nonpremixed jet flames—from CH-OH PLIF images." Combustion and Flame **122**(1): 1-19.

40. Sadanandan, R., M. Stöhr and W. Meier (2008). "Simultaneous OH-PLIF and PIV measurements in a gas turbine model combustor." Applied Physics B **90**(3): 609-618.

41. Paul, P. H. (1994). "A model for temperature-dependent collisional quenching of OHA2∑+." Journal of Quantitative Spectroscopy and Radiative Transfer **51**(3): 511-524.

42. Tu, X., et al. (2020). "Effects of temperature and pressure on OH laser-induced fluorescence exciting A–X (1,0) transition at high pressures." Chinese Physics B **29**(9): 093301.

43. Temme, J. E., A. Skiba, T. Wabel and J. F. Driscoll (2013). "Premixed turbulent combustion in high reynolds number regimes ' of thickened flamelets and distributed reactions." **3**: 2451-2457.

44. Masri, A. R., P. A. M. Kalt and R. S. Barlow (2004). "The compositional structure of swirl-stabilised turbulent nonpremixed flames." Combustion and Flame **137**(1): 1-37.

45. Meier, W., P. Weigand, X. R. Duan and R. Giezendanner-Thoben (2007). "Detailed characterization of the dynamics of thermoacoustic pulsations in a lean premixed swirl flame." Combustion and Flame **150**(1): 2-26.

46. Heinze, J., U. Meier, T. Behrendt, C. Willert, K.-P. Geigle, et al. (2011). "PLIF Thermometry Based on Measurements of Absolute Concentrations of the OH Radical." Zeitschrift für Physikalische Chemie **225**: 1315-1341

47. Harris, D. C. (1999). Materials for Infrared Windows and Domes: Properties and Performance, SPIE.

48. Lemmon, E.W., Bell, I.H., Huber, M.L., McLinden, M.O. NIST Standard Reference Database 23: Reference Fluid Thermodynamic and Transport Properties-REFPROP, Version 10.0, National Institute of Standards and Technology, Standard Reference Data Program, Gaithersburg, 2018.

49. "FM-1050 Series High Accuracy Flowmeter (150 Mm Reference), Brass." *MATHESON Online Store*, store.mathesongas.com/fm-1050-series-high-accuracy-flowmeter-150-mm-reference-brass/.

50. Engineering, Omega. “How Does a PID Controller Work?” *Https://Www.omega.com/En-Us/*, Omega Engineering Inc, 14 Oct. 2020, www.omega.com/en-us/resources/how-does-a-pid-controller-work.

51. Matthew Hay, William Swain, William Weinert, Yejun Wang, and Waruna D. Kulatilaka (2020). "Flame Instability Characterization at Elevated Pressures Using High-Speed Chemiluminescence Imaging of OH* and CH* " Central States Section of The Combustion Institute: 2020 Spring Technical Meeting.

52. Wang, Y., T. Paschal and W. D. Kulatilaka (2019). Combustion Characterization of a Fuel-Flexible Piloted Liquid-Spray Flame Apparatus Using Advanced Laser Diagnostics. ASME Turbo Expo 2019: Turbomachinery Technical Conference and Exposition.

53. Luque, J. and Crosley, D.R. (1999) **LIFBASE**: Database and Spectral Simulation Program (Version 1.5). SRI International Report MP, 99.

54. Davidson, D. F., M. Roehrig, E. L. Petersen, M. D. Di Rosa and R. K. Hanson (1996). "Measurements of the OH A-X (0,0) 306 nm absorption bandhead at 60 atm and 1735 K." Journal of Quantitative Spectroscopy and Radiative Transfer **55**(6): 755-762.

55. David G. Goodwin, Harry K. Moffat, and Raymond L. Speth. Cantera: An object- oriented software toolkit for chemical kinetics, thermodynamics, and transport processes. http://www.cantera.org, 2017. Version 2.3.0. doi:10.5281/zenodo.170284

56. Kostka, S., S. Roy, P. J. Lakusta, T. R. Meyer, M. W. Renfro, et al. (2009). "Comparison of line-peak and line-scanning excitation in two-color laser-induced-fluorescence thermometry of OH." Applied Optics **48**(32): 6332-6343.

57. Lee, T., W. G. Bessler, H. Kronemayer, C. Schulz and J. B. Jeffries (2005). "Quantitative temperature measurements in high-pressure flames with multiline NO-LIF thermometry." Applied Optics **44**(31): 6718-6728.

APPENDIX A

LabVIEW VI Figures

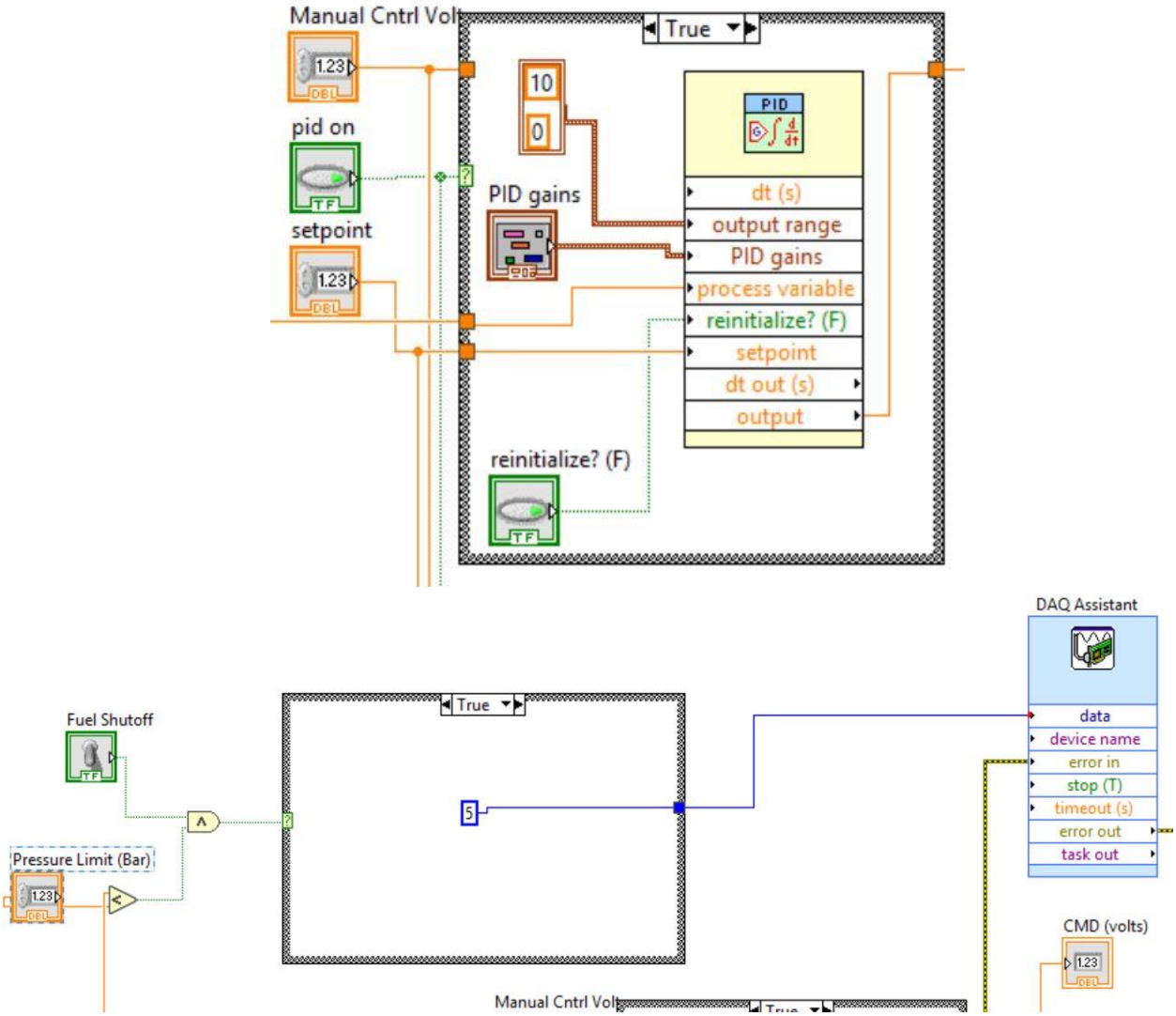

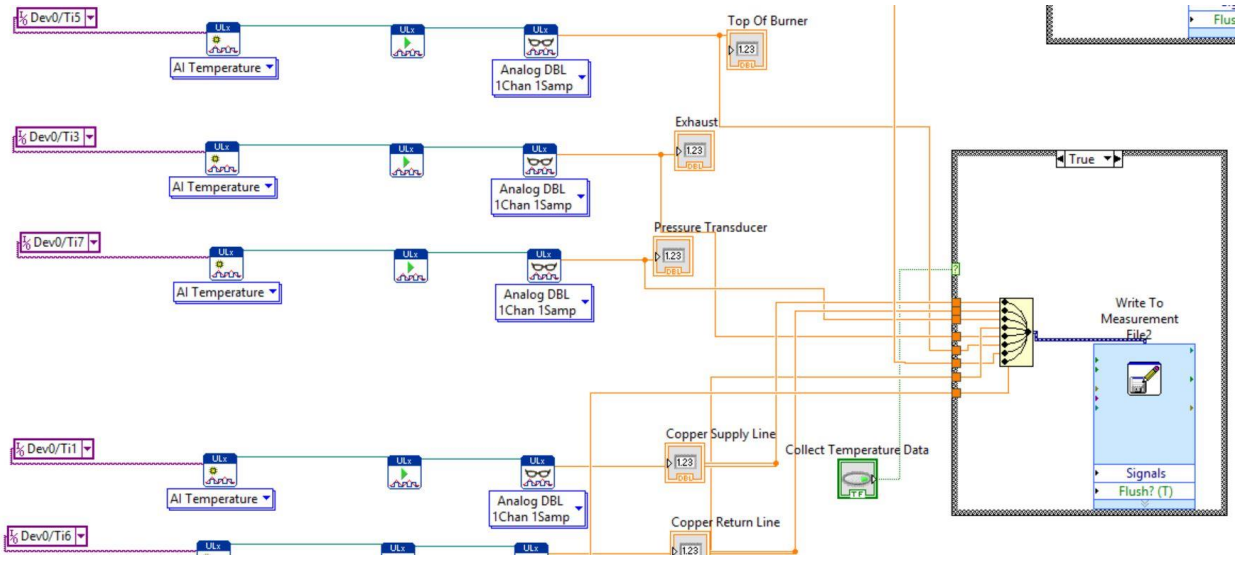
Dev0/Ti5
AI Temperature
Analog DBL
1Chan 1Samp
Top Of Burner
Dev0/Ti3
AI Temperature
Analog DBL
1Chan 1Samp
Exhaust
Dev0/Ti7
AI Temperature
Analog DBL
1Chan 1Samp
Pressure Transducer
True
Write To
Measurement
File2
Signals
Flush? (T)
Dev0/Ti1
AI Temperature
Analog DBL
1Chan 1Samp
Copper Supply Line
Collect Temperature Data
Dev0/Ti6
Copper Return Line

APPENDIX B

Mass Flow Spreadsheets

Temperatur:		298.00 K
Frischgasgeschw. - IB:		8.00 cm/s
Frischgasgeschw. - AB:		1.50 cm/s
Frischgasgeschw. - CoFl:		6.00 cm/s
ϕ	IB	1.20
λ	IB	0.83
C/O	IB	0.30

p bar (WRT Atm)	V^*_{ges} slm	$V^*_{n\text{-}CH4,IB}$ slm	$V^*_{n\text{-}L,IB}$ slm
1.00	1.36	0.152	1.212
1.50	2.05	0.228	1.818
2.00	2.73	0.305	2.424
2.50	3.41	0.381	3.030
3.00	4.09	0.457	3.635
3.50	4.77	0.533	4.241
4.00	5.46	0.609	4.847
4.50	6.14	0.685	5.453
5.00	6.82	0.762	6.059
5.50	7.50	0.838	6.665
6.00	8.18	0.914	7.271
6.50	8.87	0.990	7.877
7.00	9.55	1.066	8.483
7.50	10.23	1.142	9.089
8.00	10.91	1.219	9.695
8.50	11.60	1.295	10.300
9.00	12.28	1.371	10.906
9.50	12.96	1.447	11.512
10.00	13.64	1.523	12.118

$S^*_{n\text{-}CH4,IB}$ slm
0.119
0.178
0.238
0.297
0.357
0.416
0.476
0.535
0.595
0.654
0.713
0.773
0.832
0.892
0.951
1.011
1.070
1.130
1.189

Pressure Correction Factor (Calibrated Meters) (WRT ATM)	*Adjusted Meter Input (SLM)*	*E406 Methane* Meter Reading
0.250	0.609	12.517
0.275	0.832	15.798
0.299	1.017	18.537
0.324	1.175	20.858
0.349	1.310	22.850
0.374	1.427	24.579
0.398	1.530	26.093
0.423	1.620	27.430
0.448	1.701	28.619
0.472	1.773	29.684
0.497	1.838	30.643
0.522	1.897	31.512
0.547	1.951	32.301
0.571	2.000	33.023
0.596	2.044	33.684
0.621	2.086	34.293
0.646	2.124	34.855
0.670	2.159	35.376
0.695	2.192	35.860

Gas flow rates

Φ	Velocity (cm/s)	Pressure (Bar)	CH4 (SLM)	Air (SLM)	Air (co-flow) (SLM)
0.8	14	1	0.185	2.20	5.2
0.9	14	1	0.206	2.18	5.2
1	14	1	0.227	2.16	5.2
1.2	14	1	0.267	2.12	5.2
0.8	14	2	0.369	4.41	10.3
0.9	14	2	0.411	4.36	10.3
1	14	2	0.453	4.32	10.3
1.2	14	2	0.533	4.24	10.3
0.8	8	5	0.525	6.29	25.8
0.9	8	5	0.585	6.23	25.8
1	8	5	0.644	6.17	25.8
1.2	8	5	0.758	6.06	25.8
0.8	6	10	0.781	9.44	51.7
0.9	6	10	0.871	9.35	51.7
1	6	10	0.958	9.26	51.7
1.2	6	10	1.13	9.09	51.7

APPENDIX C

Table 2: Part List

Part	Part Number
Tigon Tubing	
Brass Instrumentation Quick Connect Body, 1.5 Cv, 12mm. Swagelok Tube Fitting	SS-QC8-B-12M0
Brass Instrumentation Quick Connect Stem with Valve, 1.5 Cv, 12 mm. Swagelok Tube Fitting	SS-QC8-D-12M0
Brass Instrumentation Quick Connect Stem with Valve, 0.2 Cv, 6 mm Swagelok Tube Fitting	B-QC4-D-6M0
Brass Instrumentation Quick Connect Body, 0.2 Cv, 6 mm Swagelok Tube Fitting	B-QC4-B-6M0
Stainless Steel Swagelok Tube Fitting, Union, 6 mm Tube OD	SS-6M0-6
1/2" 3 Piece Stainless Steel Ball Valve Threaded Ends	101212
1/2 NPT End Fitting	
1/2 NPT Fitting Tee	
1/2 Pipe for Water	
1/4 NPT PSI Pressure Gauge	4CFR6
1/2 Hose to Wall / Pump Connection	
1/4 MNPT to 1/2 Connector	
Stainless Steel Integral Bonnet Needle Valve, 0.37 Cv, 6 mm Swagelok Tube Fitting, Regulating Stem	SS-1RS6MM
1/2 HP Split-Phase Carbonator Pump Motor, 1725 Nameplate RPM, 120/240 Voltage, 48Y Frame	5KH36MNA445X
316 Stainless Steel Nut for 12 MM Fitting	SS-12M2-1
316 Stainless Steel Front Ferrule for 12 mm Swagelok Tube Fitting	SS-12M3-1
Stainless Steel Swagelok Tube Fitting, Reducing Union, 12 mm x 6 mm Tube OD	SS-12M0-6-6M
Stainless Steel Poppet Check Valve, Fixed Pressure, 6 mm Swagelock Tube Fitting, 1 psig	SS-6C-MM-1
Stainless Steel Swagelok Tube Fitting, Union Tee, 6 mm Tube OD	SS-6M0-3
PTFE-Lined, Stainless Steel Braided Hose Assembly, 6mm Stainless Steel Swagelock Tube Adapters, 34.7 in Live Length	SS-4MBHT-36
Stainless Steel All-Welded In-Line Filter, 6 mm Swagelok Tube Fitting, 0.5 Micron Pore Size	SS-6FWS-MM-05
Stainless Steel Swagelok Tube Fitting, Bulkhead Union, 6 mm Tube OD	SS-6M0-61
Stainless Steel Swagelok Tube Fitting, Union, 6 mm Tube OD	SS-6M0-6
Stainless Steel Poppet Check Valve, Fixed Pressure, 12 mm Swagelok Tube Fitting, 1 psig (0.07 bar)	SS-12C-MM-1
Relief Valve (With Burst Disk) Rembre	
316 Stainless Steel Nut and Ferrule Set (1 Nut/1 Front Ferrule/1 Back Ferrule) for 6 mm Tube Fitting,	SS-6M0-NFSET
316 SS Nut and Ferrule Set (1 Nut/1 Front Ferrule/1 Back Ferrule) for 12 mm Tube Fitting,	SS-12M0-NFSET
Heavy-duty tubing PAN-R-6X1,1-SI	541675
Stainless Steel Integral Bonnet Needle Valve, 0.37 Cv, 6 mm Swagelok Tube Fitting, Regulating Stem	SS-1RS6MM
12mm Tubing Mcmaster Carr	9811T15
6mm Tubing Mcmaster Carr	9811T12
Yor-Lok Fitting for Stainless Steel Tubing Straight Adapter for 6mm x 1/4" Tube OD	5305K302
UR484802-Temperature DAQ	18X4963
6 mm Tube Bender	38053
Red Control Valve	
K-Type Thermocouple	
Omega 4-20 mA Converter	DRF-VAC-115VAC-15V-0/10

National Instruments USB-6008	6008
SSLM1D23BD - Solid State Relay, SPST-NO, 3 A, 60 VDC, DIN Rail, Screw	SSLM1D23BD
Power Relay, SPDT, 24 VDC, 10 A, G2RS Series, Socket, Non Latching	G2R-1-S-DC24(S)
Power Supply 24V 20A 500W AC 96V-240V Converter Adapter DC S-500W-24 Power Supply	
Chemical-Resistant Viton® Fluoroelastomer O-Ring Super-Resilient, 2 mm Wide, 5 mm ID Mcmaster Carr	1295N223
Chemical-Resistant Viton® Fluoroelastomer O-Ring Super-Resilient, 2 mm Wide, 60 mm ID Mcmaster Carr	1295N268
Chemical-Resistant Viton® Fluoroelastomer O-Ring 2 mm Wide, 80 mm ID Mcmaster Carr	9263K669
Chemical-Resistant Viton® Fluoroelastomer O-Ring Super-Resilient, 3 mm Wide, 60 mm ID Mcmaster Carr	1295N338
Chemical-Resistant Viton® Fluoroelastomer O-Ring Super-Resilient, 2.5 mm Wide, 25 mm ID Mcmaster Carr	1295N312
Chemical-Resistant Viton® Fluoroelastomer O-Ring Super-Resilient, 2.5 mm Wide, 78 mm ID Mcmaster Carr	1295N501
Chemical-Resistant Viton® Fluoroelastomer O-Ring Super-Resilient, 3 mm Wide, 75 mm ID Mcmaster Carr	1295N341
Chemical-Resistant Viton® Fluoroelastomer O-Ring 3 mm Wide, 85 mm ID Mcmaster Carr	9263K752
Chemical-Resistant Viton® Fluoroelastomer O-Ring Super-Resilient, 3 mm Wide, 34 mm ID Mcmaster Carr	1295N561
3X92.00 METRIC O-RING 4.4300 EA 13.29 VITON (FKM) 75 DURO BLACK Global O-Ring	
3X83.00 METRIC O-RING 2.3200 EA 9.28 VITON (FKM) 75 DURO BLACK Global O-Ring	
2.4X33.30 METRIC O-RING 2.5000 EA 62.50 VITON (FKM) 75 DURO BLACK Global O-Ring	
O Ring 13.6 x 3	
O Ring 29.1 x 2.55	
O Ring Tool, 2 Pieces	4F418

APPENDIX D

Operating Procedure:

- Plug in all electrical components and turn on the power strip.
- Make sure the motor is effectively running and no water leaks are present in the system, and check the inside of the burner to make sure no excess water is running through the system.

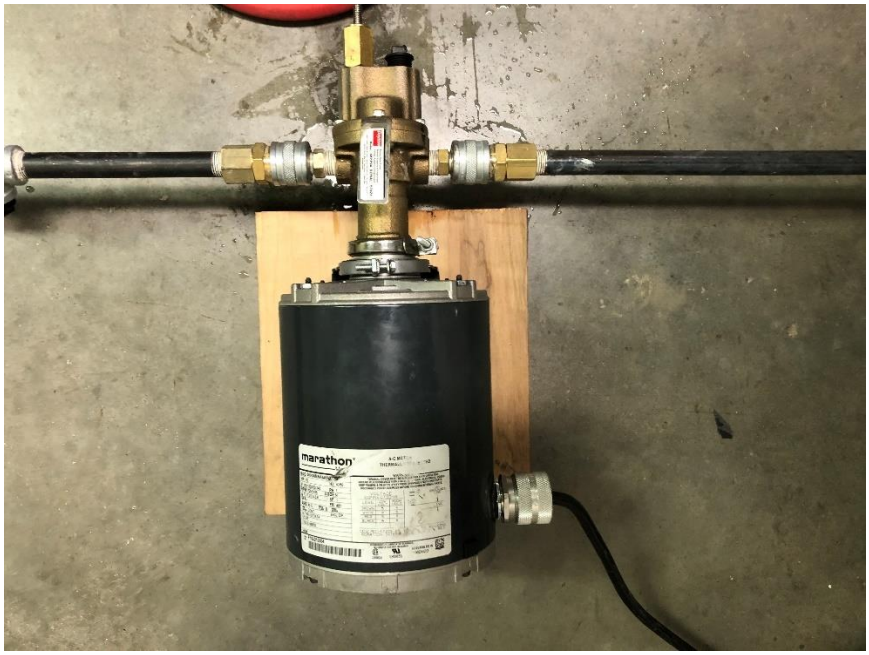

Water Pump to Drive Water System

- Turn on the shop air and regulate the valve to where the pressure is 110 psi.
- Close both water condensation lines attaches to the midsection and bottom of the burner in order to stop the flow of air leaking during testing.
- Make sure all mass flow control valves are closed upon starting the experiment so that the gases do not start flowing unexpectantly though the combustor.

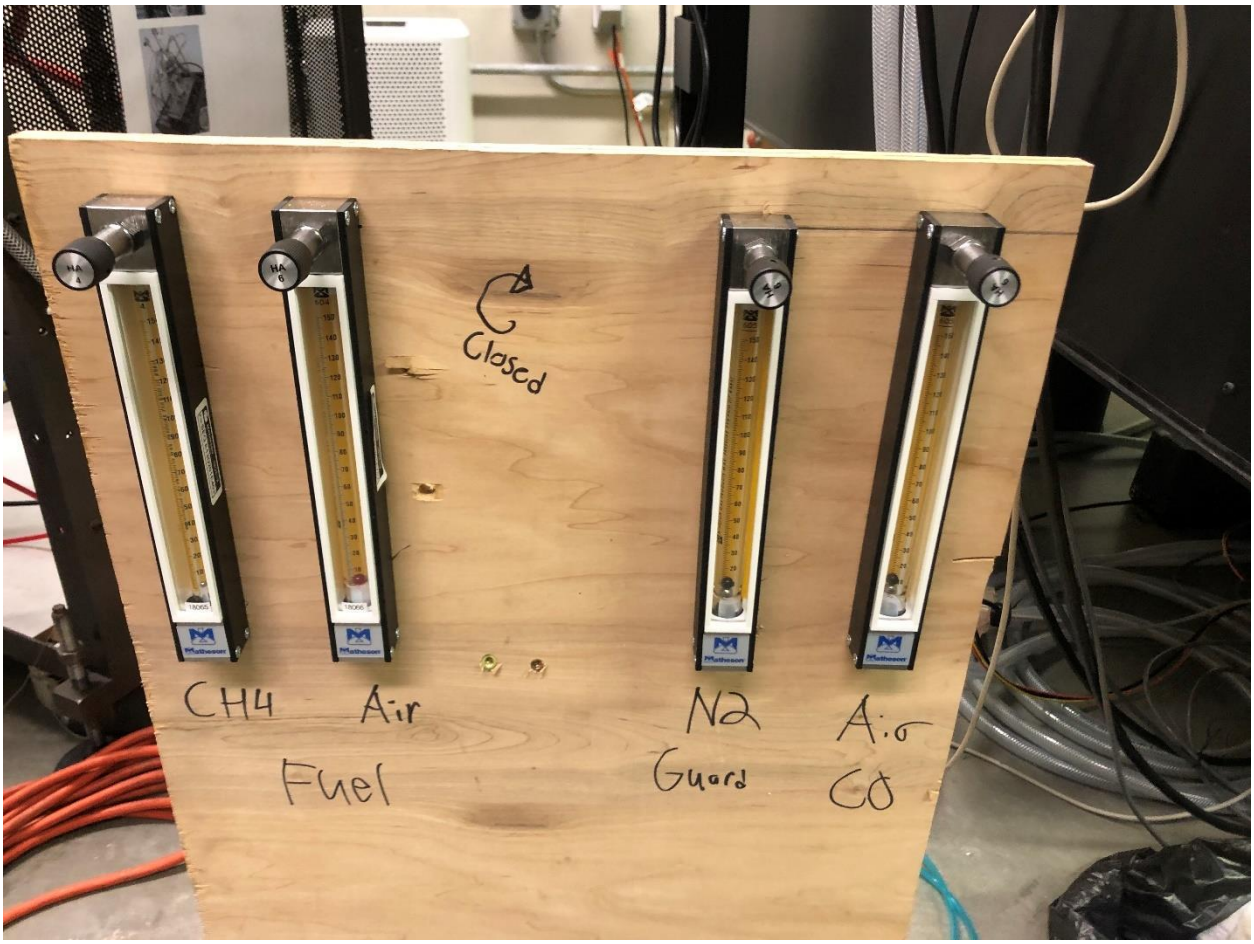

Co-Flow and Guard Flow Controller Setup

- Make sure all mass flow control valves are closed upon starting the experiment so that the gases do not start flowing unexpectantly though the combustor.
- Start the LabVIEW VI and go to the front panel.

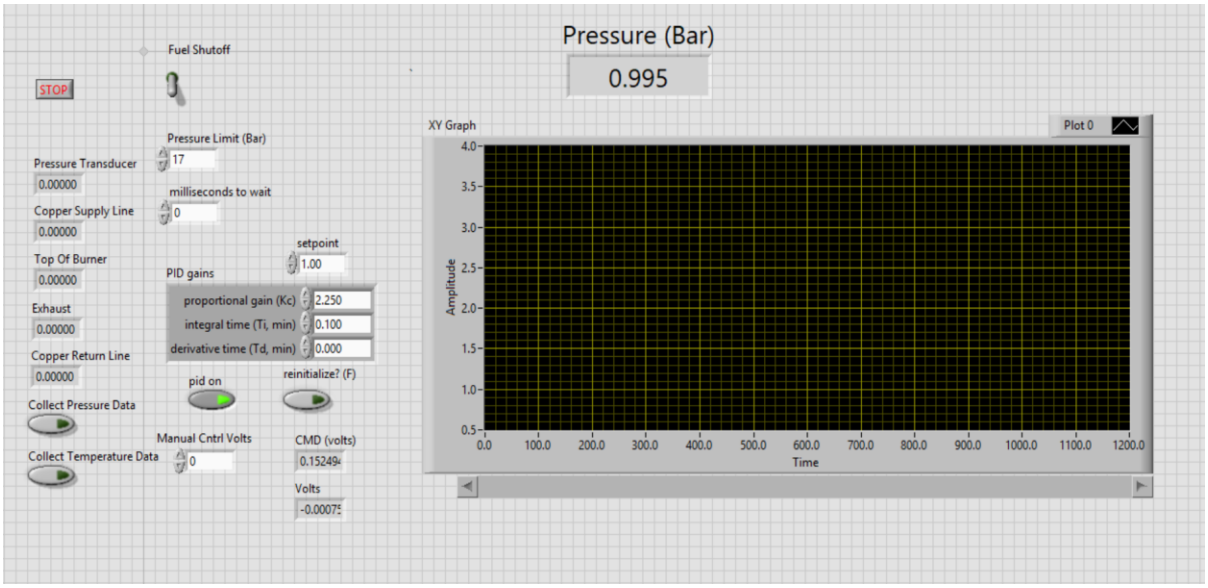

Control System and Data Acquisition

- LabVIEW Test Setup Section

  1. Set the Pressure Limit to be 12 Bar for Tests at 10 bar and 17 bar for pressure tests at 15 bar.
  2. Set the proportional gain to be 2.250, the integral time to be .1, and the derivative time to be 0.
  3. Change the setpoint to be .95 Bar so the controller will be at the starting state.
  4. Start the VI and hit run.
  5. Hit the buttons to collect both pressure and temperature data.
  6. Turn on the PID control and flip the fuel shutoff to off.

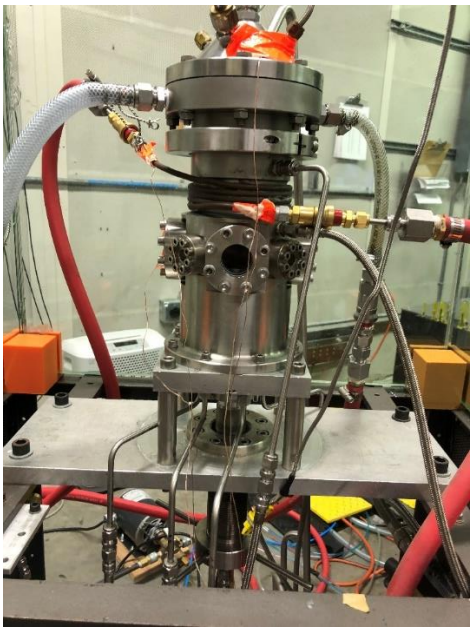

High Pressure Burner

- Beginning of Flame Operation and Ignition

1. Open all gas bottles to 40 psi and make sure that the mass flow controllers are all closed.
2. Remove the back panel and remove the optical window viewer with the aluminum blank.
3. Open the mass flow controllers for only the air and fuel mixture to their corresponding flow rates for 1 atm and an equivalence ratio of 1.2.
4. Ignite the flame by using a lighter. Place the lighter inside of the vessel and attempt to ignite, if that does not work light the lighter outside of the vessel and then reach back into vessel.
5. Once the flame is stable and the guard and co-flow have been opened up on the mass flow controllers, put the window back onto the vessel and place the blast shield back in its holder.
6. The flame should be stable at this point, the next step is to pressurize the vessel.

- Pressurization Procedure

1. The procedure will involve varying the pressure in the gas bottles and adjusting the mass flow controllers and LabVIEW code accordingly. The pressure adjustments will be made in increments of .5 bar in order to not cause mini explosions due to high pressure jumps.
2. When the flame is lit at 1 atm and all safety procedures have been undertaken, open all of the gas bottles to 15 psi more than the previous setpoint. One person should be adjusting the gas bottles and another should be using the mass flow controllers to regulate the flame.
3. Adjust the air fuel mixture to the next pressure step on the MKS controller, for example; if starting at 1 bar adjust air / fuel ratio to 2 bar at equivalence ratio of 1.2.
4. Increase the guard and co-flow to the rates for 2 bar.
5. Adjust the LabVIEW pressure control to 1.5 bar
6. Readjust the guard and co-flow up to 2 bar as they will have dropped due to the increase in backpressure.
7. Repeat this procedure until reaching the desired pressure of 10 or 15 bar.

- Shutdown Procedure

1. Hit the fuel shutoff control in LabVIEW.
2. Hit .95 bar on the pressure controller to fully open the valve while simultaneously closing the pressure valves on all the bottles to let the burner bleed out excess fuel and air. Also open all MKS MFC's to fully open but keep the LABVIEW fuel shutoff closed
3. Reopen fuel shutoff when all other gases are drained but methane.
4. Close mass flow controllers.
5. Turn off water pump
6. Open water condensation valve to let excess water out.
7. Inspect windows and burner for damage.
8. Turn on ventilation fan in room and let ventilate.